Sky Cruiser – A Design Study in Space Tourism

Joshua H. Heinz[1], Kevin P. O'Brien[1], Tyler L. Hatch[1], Daniel Kosednar[1], Andrew Jones[1], Rylan Schwan[1]

and

Timothy T. Takahashi[2]

Arizona State University, Tempe, Arizona, 85281

This paper documents the Model Based Systems Engineering design methodology, process, and results for a study in the development of a mixed propulsion, unitary, 14 CFR § 25 compliant space-tourism vehicle. *ModelCenter* was utilized to connect several developed tools together and to run trade studies. We propose a 6-passenger, 131,000-lbm MTOW, high wing with two top-mounted turbofan engines and an aft mounted RP1/LOX rocket motor, and a T-Tail configuration. It can fly for 129 seconds above the 50-mile line with a peak altitude of approximately 332,000-ft. The vehicle experiences a maximum Mach Number of 3.77 on re-entry.

[1] Undergraduate Student, Aerospace Engineering, School for Engineering of Matter, Transport and Energy, PO Box 8576016, Student Member AIAA.
[2] Professor of Practice, Aerospace Engineering. School for Engineering of Matter Transport and Energy, PO Box 8576106, Associate Fellow AIAA

I. Introduction

THE boundary of space has long been a point of interest for scientists, engineers, and the general public. Attempts to create a rocket plane are well documented, from the esteemed X-15 to the more recent SpaceShipTwo. The recent interest in space tourism drives our goal to consider what a **unitary**, rather than staged, aircraft needs to look like that can take off and land as a conventional aircraft and fly quasi-ballistic trajectories that breach the internationally recognized boundary of space. This paper details a conceptual design of such an aircraft developed using a model-based systems engineering approach. Our aircraft, the *Sky Cruiser*, is a mixed propulsion (rocket and turbofan) powered airframe with a T-Tail, a highly swept wing with top mounted engines.

II. Concept of Operations

As referenced above, this paper explores the design of a 14 CFR § 25 [1] compliant vehicle capable of traveling above the von Kármán line, the internationally recognized boundary of space. Our goals differ from other examples of vehicles that breach the boundary of space in that this design is a unitary one, meaning that all phases of the mission are accomplished by a singular vehicle; unlike the X-15 (air-dropped from a B-52) or the SpaceShipTwo (air-dropped from SpaceShipOne).

A single airframe must be able to takeoff and climb to some sort of cruise altitude, ignite its rocket and fly a near ballistic trajectory into and back from outer space, recapture air breathing propulsion, and fly back to its home airport. Per FAA regulations, it must also be able to balk a landing at the primary airport, fly to a diversion runway and perform a 45-minute hold. Each segment of this mission provides key parameters that were calculated and optimized to ensure a valid overall configuration, both physically and legally.

The validity of a configuration was determined through a set of Key Performance Parameters (KPP), Measures of Performance (MOP), as well as Measures of Effectiveness (MOE). KPPs considered included the vehicle weights (*MTOW, MLW, OEW*, and fuel weight), thrust and drag, and ISP. Measures of Performance included the apex altitude of the flight, time above the von Kármán line, as well as the takeoff and landing distance of the vehicle. The primary MOEs used were the mission weight per passenger, rocket fuel burnt per jet fuel burnt, and compliance with the Code of Federal Regulations. Every facet of the design process kept these KPP, MOP, and MOE in mind to ensure a complete and effective design at completion.

Some specific aspects of our mission were predefined, while the vast majority were determined through extensive testing. It was necessary to ensure the design of a trimmable and controllable aircraft. A successful design demonstrates stability in the "A" region of the Bihrle-Weissman Chart [2] and controllability through a level 1 grade via MIL 8785C [3]. Additionally noted, that even though the climb to space will require supersonic flight where shocks will be impossible to avoid, the wing should be designed such that while in cruise no shocks will form.

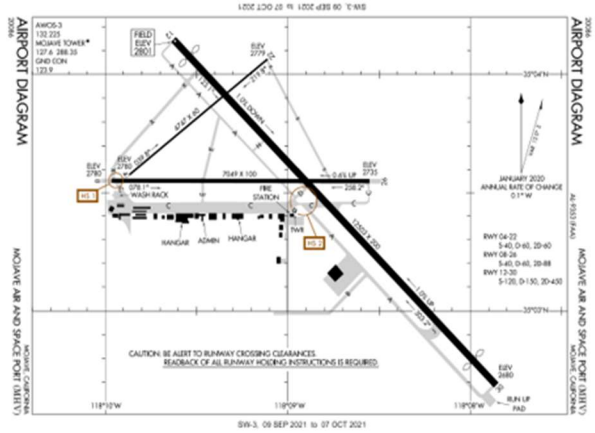

FIGURE 1. Mojave Air and Space Port Runway Diagram

To begin, a hub was designated to function as the model airport that our vehicle will function out of. The hub chosen was Mojave Air and Space Port, seen in FIGURE 1 for its proximity to the coastline, the long runways, and existing infrastructure for handling and usage of rocket fuel. It was critical for the airport to be close to the coast to help reduce the weight requirements for the mission phases prior to rocket ignition because supersonic flight over land in the United States is prohibited by 14 CFR § 91.817 [1]. After takeoff and climb to cruise altitude towards and past the coast, the vehicle would turn back toward Mojave Air and Space Port just prior to the rocket ignition. Re-entry occurs with ample time for speed to be reduced well below the legal limit before passing over land, where a typical airbreathing propulsion powered descent to landing would then be completed.

This design study was intended to be an exploration of the capabilities and requirements for a space vehicle, and not into the intricacies of the design of a rocket engine. As such, it was clear that for the purpose of this design, an off the shelf rocket was to be chosen that best fit the needs of the final vehicle. The engine of choice was the oft-used Merlin 1D+ engine, with further justification to come later.

The proposed mission includes a period when the aircraft will be at the edge of space, in low-density, low-pressure conditions. This time at the edge of space brings special requirements to the proposed aircraft related to maneuverability, pressurization, and cabin power. At the edge of space, the conditions are such that maneuvering the aircraft via typical aerodynamic control surfaces will have almost no effect. This occurs because the dynamic pressure approaches zero in this region.

Space vehicles often use small gas thrusters to perform maneuvers while in orbit; this aircraft also utilizes thrusters for maneuvering. The MONARC-445 is used in this design because it is lightweight and can provide up to 234-sec of thrust, which is more than sufficient for this mission [4].

At these high-altitude conditions, the plane is also at risk of a major decompression. 14 CFR § 25.841 [1] breaks down requirements for maintaining cabin pressurization. Applicable to this aircraft is (a)(1) which states that the vehicle must not allow passengers to experience pressure altitudes greater than 15,000-ft if the plane is certified for over 25,000-ft in altitude. To mitigate this risk, all passengers will be supplied with pressure suits so that in the event of decompression, they are kept safe despite the extreme pressure differential.

Doing this ensures CFR compliance and reassures passengers that steps are being taken to protect them. Typical airplanes utilize air-breathing systems to run electrical generators for onboard power and battery charging. During the space-flight portion of the mission, air-breathing engines will be turned off and shrouded. At this time, the aircraft will have to rely purely on batteries to maintain power to onboard avionics, lighting, and cabin systems. 14 CFR § 25.1353(b) [1] defines battery specific requirements. The design of batteries is outside the scope of this study; however, a series of typical nickel-cadmium battery should be sufficient for this mission [5].

III. Development of Design Tools

To facilitate the design of a vehicle capable of completing the intended mission, we developed a series of tools. These tools, described in the following sections, were created to work together to demonstrate a clear picture of the capabilities of any given configuration.

A. Weight Sheet

An empirically driven weight sheet was used utilizing resources from Torenbeek's weight regressions [6] as well as Takahashi [7] to determine values such as the structural component weights, propulsion system weights, and other system weights to determine the Operational Empty Weight (*OEW*) for a given Maximum Takeoff Weight (*MTOW*) and various geometric inputs for a vehicle. The empirical estimates used to determine these weights were based on transport category airplanes, which may have called into question the validity of such a tool for a supersonic rocket plane such as this project necessitates.

To accommodate for this, an empirical estimation of rocket and rocket-associated weights from Veetil [8] was incorporated to the existing weight estimation tool. This tool was configured to determine the proper sizing of tank for a mass of fuel, and the total length of the system including the oxidizer tank, fuel tank, and thrust chamber length. An empirical method for determining the length of the thrust chamber can be seen in Eq. 1, which depends solely on the thrust output of the engine.

$$l_{tc} = (3.042 \times 10^{-5} T + 327.7) \times 10^{-2} \qquad \text{Eq. 1}$$

The mass of the thrust chamber, also dependent on the thrust of the engine, was empirically determined using the relationship in Eq. 2.

$$m_{tc} = \frac{T}{g_0(25.2\, log\, log\, T\ - 80.7)} \qquad \text{Eq. 2}$$

The wide range of properties for propellants that could be chosen precluded a need for a tool to determine the tank weights based on those fuels and oxidizers specifically. Thus, from the ideal oxidizer-to-fuel ratio and total propellant mass came the mass of the oxidizer and fuel specifically, as shown in Eq. 3.

$$m_{prop} = m_f + m_{ox} = m_f(O/F^* + 1) \qquad \text{Eq. 3}$$

A tank designed with a cylindrical body with semi-spherical end caps was assumed, and the weight estimation for each of those sections are shown in Eqs. 4-5, which were applied to both the oxidizer and fuel tanks.

$$m_{cyllindrical} = \rho_{mat} l_c \pi \left[\left(\frac{d_{tk}}{2}\right)^2 - \left(\frac{d_{tk}}{2} - \delta_{cyllindrical}\right)^2\right] \qquad \text{Eq. 4}$$

$$m_{spherical} = \frac{4\rho_{mat}\pi}{3}\left[\left(\frac{l_s}{2}\right)^3 - \left(\frac{l_s}{2} - \delta_{spherical}\right)^3\right] \qquad \text{Eq. 5}$$

The wall thickness, δ, for the tanks was determined from the Eqs. 6-7, accounting for burst pressure and the material strength.

$$\delta_c = \frac{0.5 p_b d_{tk}}{F_{tu}} \qquad \text{Eq. 6}$$

$$\delta_s = \frac{0.25 p_b d_{tk}}{F_{tu}} \qquad \text{Eq. 7}$$

Burst pressure was calculated using a safety factor, operating pressure ratio, and can be seen in Eq. 8. Here V_{tk} is the volume of the tank, with an ullage of ten percent.

$$p_b = \eta_s \lambda_b p_{tk} = \eta_s \lambda_b \left\{10^{-0.1068[loglog\ (V_{tk})\ -0.2588]}\right\} \times 10^6 \qquad \text{Eq. 8}$$

Lastly the structural mass for the rocket propellant system was estimated using Eq. 9, which completed the mass build-up.

$$m_{st} = 0.88 \times 10^{-3} \times (0.225T)^{1.0687} \qquad \text{Eq. 9}$$

To check for validity, known values of the X-15 published weights [9] were compared to our weight sheets predictions, and were within a satisfactory range to the authors. The validated weight estimation of a vehicle configuration was then used for various other tools outlined below.

B. *EDET*

In order to develop an aerodynamic database, the Empirical Drag Estimation Technique (*EDET*) [10] was used. *EDET* is a tool developed by Lockheed in conjunction with NASA to determine drag coefficients and was used to develop a planform that minimizes drag as well as evaluate performance. *EDET* provides valid drag estimates up to Mach 3 inside practical atmospheric limits (~200,000-ft). This was deemed sufficient for this study as the periods of our flight that exceed these limitations occur at low dynamic pressure.

C. *VORLAX*

VORLAX [11, 12, 13] is a combined subsonic / supersonic vortex lattice method potential flow solver, from which accurate pressure distributions, lift coefficients, and induced drag characteristics can be calculated from a geometric input. A method was developed for automatically generating a geometry to be run through *VORLAX*. Initial iterations consisted of flat plate panels, which were later improved to sandwich panel models to properly determine twist and camber distributions across the span.

D. Sky Maps

A point performance "sky maps" tool was developed to inform the mission planning of a completed design for our aircraft. Given the 5-column engine data and *EDET* output files, this tool gives contour plots of chosen parameters, in this case the KEAS, *KTAS*, *M(L/D)*, specific range, constant Mach rate of climb, and constant ROC at various Mach Numbers and altitudes. Most importantly, these contour plots were used to determine the optimal climb settings. This tool yielded valuable insight to the certifiability of our designs (given the CFR regulations concerning climb) as well as measure their effectiveness through the specific range through the entirety of the aircraft's mission among other parameters [1].

E. Mission Code

A Mission Performance Code was developed by Griffin & Takahashi [14] to evaluate the performance of a vehicle over each stage of a mission. Utilizing an *EDET* drag build-up, 5-Column propulsion data, and a mission script, this tool simulates and provides data about the mission it ran. The ability to change propulsion files, as was critical due to our mission requiring a rocket powered segment in addition to an air-breathing jet powered segment, was added. Callouts to the peak temperatures, both stagnation and equilibrium wall temperature, were added along with reporting times above thresholds deemed important to material integrity. Peak altitudes and times above the relevant flight levels critical to mission success were reported, as well as reporting of the *nZ* based on both the *MTOW* and current weight during the mission. Successful cases run through the mission code were limited to those that did not exceed Mach 4 to ensure that data is reliable, due to the limited accuracy of our aerodynamic databases above that threshold. This tool was the primary method for evaluating the performance of our various configurations tested throughout the design study, ensuring our vehicle achieved the speed and altitude performance milestones as well as having enough available fuel to complete the mission.

F. Wing Thickness & Skin Thickness Chooser

To design an efficient and high performance a wing, a method for determining the desired thickness was deemed a requirement. From this requirement the Thickness Chooser tool was born. For a given weight, design Mach Number, altitude, and planform geometry, a spanwise distribution of the running load (*L'*) was calculated. This led directly to the spanwise lift coefficient (*Cl(y)*) being determined. Then, the sweep modified Korn equation [15] was used to determining the maximum allowable thickness at chosen spanwise locations. In addition to *L'* informing the overall thickness of the wing along the span, it was used in conjunction with the maximum loading (*nZ-max*) seen in the mission to determine the skin thickness requirements of the wing.

G. Wing Geometry Tool

The tools presented above provided an acceptable starting point for much of the necessary geometry of the wing. The determined geometries were implemented into a new tool to perform a detailed design. Utilizing *VORLAX* as noted previously, a wing and fuselage model was generated, including the wing as a sandwich panel with variable thickness, camber, and twist, and the fuselage as two horizontal flat plates. Five leading edge control points were defined across the semispan of the wing from side of body to tip (FIGURE 2), defining each airfoil cross section. The main purpose of this tool was to design a suitable wing which: meets its lift design criterion, meets its critical Mach Number criterion, exhibits an elliptical lift distribution at the design lift coefficient and Mach Number, and produces favorable isobar patterns.

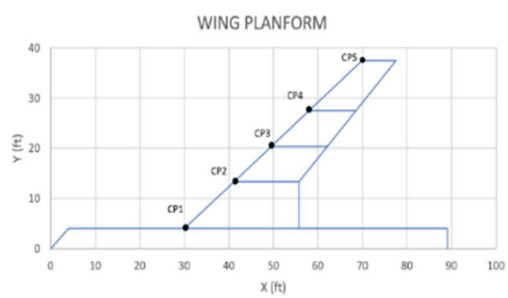

FIGURE 2: Wing Geometry and Control

To determine if the wing provided adequate lift, the lift coefficient calculated from *VORLAX* was compared to the design lift coefficient at cruise calculated in Eq. 10, assuming a fully loaded aircraft with a weight equal to the previously specified MTOW. This allowed for a convenient check of the wing's lifting capability and was automatically updated with changes in the wing geometry. The *VORLAX* calculated lift coefficient is highly dependent upon the set angle of attack of the model.

$$C_{L_{design}} = \frac{W}{q \cdot S_{ref}} \qquad \text{Eq. 10}$$

It is well known that when a strong shock wave forms over the wing surface, it can trigger separated flow, which results in a large increase in drag. This is undesirable at the cruising conditions of this mission. The pressure coefficient indicating a critical Mach Number on the upper surface was found through calculation of Küchemann's critical pressure coefficient (c_p*) seen in Eq. 11 [15].

$$c_p* = \frac{2}{\gamma M_\infty^2}\left\{\left(\frac{2}{\gamma+1}\right)^{\frac{\gamma}{\gamma-1}}\left(1+\frac{\gamma-1}{2}M_\infty^2\Lambda\right)^{\frac{\gamma}{\gamma-1}}-1\right\} \qquad \text{Eq. 11}$$

The airfoil geometry at each control point of the model was assigned variable thickness, camber, and twist. As suggested by Kurus & Takahashi, negative camber was assigned at the side of body to "help improve pressure isobar alignment over the span of the wing" [16] and to promote suitable stall characteristics.

To minimize the induced drag of the wing, the ideal loading was determined through Eq. 12, to be compared with the actual loading calculating from this tool [7]. The distribution of lift was then able to be tailored to the ideal one through modification of the designed twist, camber, and thickness at the various control points across the span.

$$L'(y) = 1.226 \cdot \sqrt{1 - \left[\frac{y}{b\,/\,2}\right]^2} \left(\frac{W}{S}\right) \underline{c} \qquad \text{Eq. 12}$$

While 2-D theory often implies one can neglect spanwise flow of a swept wing, recent work seen by Kirkman & Takahashi [17] suggests that when determining the local critical pressure coefficient, it is necessary to consider properties of the flow other than the Mach Number "normal to the leading edge". For these reasons, isobar unsweeping was controlled as far across the span as possible, to enhance the benefits of the wing's high leading edge sweep angle. Peak suction and isobar inclination is shown to closely align with the leading-edge sweep angle, implying the wing will succeed in avoiding wave drag disadvantages stemming from irregular isobar patterns [16]. Controlled by choice of thickness, camber, and twist, the isobar pattern of the wing was of high importance in the design process. This tool allowed for the geometry of a wing to be varied until the performance met all the requirements for the proposed mission.

H. Stability and Control Tool

To begin the stability analysis, a panel model of the aircraft was created for use with *VORLAX*. This panel model was then reproduced with various control surface deflections to obtain the five necessary input files to run a complete stability case. The first file consists of the basic aircraft configuration with no sideslip angle. The second file consists of the basic aircraft configuration with 1 -deg of sideslip. The next three files correspond to a single control surface being deflected 30-degrees at no sideslip (i.e., elevators, rudder, and ailerons). Each of these files follow the Boeing notation for obtaining positive moments. For rudder deflection, the trailing edge is deflected to the pilots right. For the elevators, the trailing edge is deflected down. For the ailerons, the right aileron deflects its trailing edge up and the left is deflected down. For each configuration files, a set of Mach Numbers and angles of attack are defined. All the files are then run, and key aerodynamic derivatives are obtained. With these five output files, the data is first imported and parsed into a Microsoft Excel sheet for further post processing.

From these stability derivatives, a series of important cue speeds are calculated for a variety of TOWs correspond to; half jet fuel + no rocket fuel, full fuel jet + no rocket, full jet + half rocket, and finally full jet and full rocket. The speeds of interest are stall speed, minimum control ground speed, minimum control air speed, crosswind, and *V2* speed. Another limitation in this section was set by 14 CFR § 25.237 [1], where the aircraft must be able to trim out at least 25-knots at scheduled takeoff (*V2*) and landing (*Vref*) speeds. From these cue speeds, the aileron was sized to ensure this regulation was met. The other key regulations require safe flight with one engine inoperative. [1] The equations for the key cue speeds are shown in Eq. 13 through 20 [7].

$$V_s = \sqrt{\frac{\frac{W}{S}}{1481 * CL_{max_{Flaps}}}} * 660.8 \qquad \text{Eq. 13}$$

$$V_{ref} = max(1.23\, V_s, VMCL) \qquad \text{Eq. 14}$$

$$VMCG = \sqrt{\frac{T * y_e}{1481 * S_{ref} * b * \left(\frac{dC_n}{drud}\right) \delta_{rud}}}\ 660.8 \qquad \text{Eq. 15}$$

$$\beta_{aileron} = \frac{\left(\frac{dC_L}{d_{ail}} * \delta_{ail}\right)}{\frac{dC_L}{d_\beta}} \quad \text{Eq. 16}$$

$$\beta_{rudder} = \frac{\left(\frac{dC_n}{d_{rud}} * \delta_{rud}\right)}{\frac{dC_n}{d_\beta}} \quad \text{Eq. 17}$$

$$VMCA_{rudder} \approx \sqrt{\frac{(T * y_e)}{1481 * \left(\left(\frac{dC_n}{db}\right) * \frac{\left[\left(\frac{dC_l}{dail}\right)\delta_{ail}\right]}{\frac{dC_l}{d\beta}} + \left(\frac{dC_n}{d_{rud}}\right)\delta rud\right) S_{ref} * b}} * 660.8 \quad \text{Eq. 18}$$

$$V_{crosswind} = sin\left(min\left(\beta_{max_{rudder}} . \beta_{max_{ailerions}}\right)\right) * \sqrt{\frac{1481}{\frac{q}{M^2}(ALT)}} * \left(\frac{KIAS}{660.8}\right) * a(ALT) * 0.592 \quad \text{Eq. 19}$$

$$V2 = max(1.13 * V_s,\ 1.1 * VMCA) \quad \text{Eq. 20}$$

Also, from the aerodynamic coefficients obtained from *VORLAX*, stability parameters could then be calculated. The first parameters to examine were the stick fixed parameters: lift curve slope, the pitching, yawing, rolling moments and side force. These parameters were plotted to determine if the static stability requirement was met. The static margin is then calculated using Eq. 21 [7] to ensure that the aircraft is stable throughout the flight with some movement in the center of gravity location.

$$SM = -\frac{dC_m}{dC_L} * 100\% \quad \text{Eq. 21}$$

The next parameter of interest was the trim power of the horizontal tail. An all moving horizontal tail was chosen for this aircraft due to the sufficiently large control power required at supersonic speeds. To calculate the elevator deflection required to trim Eq. 22 [7] was used.

$$\delta_{elevator} = \frac{C_m}{\frac{dC_m}{d_{elevator}}} \quad \text{Eq. 22}$$

To begin the longitudinal and lateral-directional stability analysis, a flight path is first needed. From the mission code a series of Mach Number and altitude pairs are obtained. From these Mach and altitude pairs, dynamic pressure (Eq. 23) and knots equivalent airspeed (Eq. 24) are calculated using standard atmosphere values obtained from Mason's ATMOS 76 programs in VBA. [18] Using the dynamic pressure and the reference area of the aircraft wing, the dimensional lift can be converted into a non-dimensional lift coefficient using Eq. 25.

$$q = \frac{q}{M^2} * M^2 \quad \text{Eq. 23}$$

$$KEAS = 660.8 * \sqrt{\frac{q}{1481\ (lbf/ft^2)}} \quad \text{Eq. 24}$$

$$C_L = \frac{L}{q * S_{ref}} \quad \text{Eq. 25}$$

This flight lift coefficient represents the lift coefficient of the aircraft at the given Mach and altitude pair. To obtain accurate data at this lift coefficient, the output data needs to be interpolated as only a finite number of Mach Numbers and angles of attack cases were run. To obtain accurate data, a double interpolator was created to calculate data between the various cases run in *VORLAX*. The first step of this interpolator was to determine which *VORLAX* Mach Numbers bounded the flight number and split them into an upper and lower bound. The data was then combed through to determine an upper and lower bound for the flight lift coefficient. The linear interpolation formula was then applied to determine both an upper angle of attack and lower angle of attack.

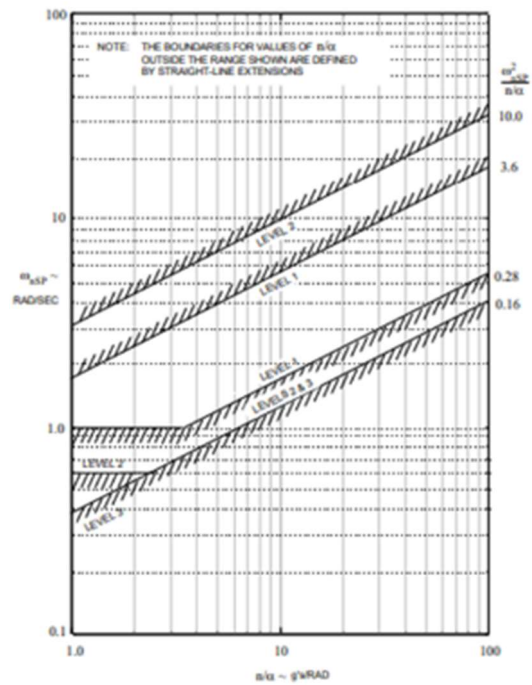

FIGURE 3 MIL STD 8785C Category A chart [3]

With the upper and lower trim angles of attack found, a final interpolation could be completed between the upper and lower Mach Number bounds to obtain the true corresponding angle of attack that goes with the flight lift coefficient. In this final interpolation the coefficients *dCm/dα* and *dCl/dα* were calculated as they are only a function on Mach Number. Due to a combination of gridding issues, supersonic vs subsonic flow interference, and taper ratio problems, the spacing between the Mach Number cases ran is quite high so this process was necessary in obtaining more accurate estimation for the given flight conditions.

With the flight lift coefficient and pitching moment slopes found, the Short Period frequency could be calculated. Equation 26 gives the Short Period frequency in hertz and Eq. 27 is used to calculate the pitch responsiveness [7]. To determine the longitudinal flight handling characteristics, the military standard MIL STD 8785C was utilized shown in FIGURE 3 [3].

$$\omega_{SP} = \frac{1}{2\pi} * \sqrt{\frac{\left(-57.4\left(\frac{dCm}{d\alpha}\right) * q * S_{ref} * \underline{c}\right)}{I_{yy}}} \qquad \text{Eq. 26}$$

$$\frac{n}{\alpha} = \frac{\left(57.4 * q * S_{ref} * \left(\frac{dCL}{d\alpha}\right)\right)}{W} \qquad \text{Eq. 27}$$

Using the *VORLAX* data, the parameters $C_n\beta\ dynamic$ shown in Eq. 28 and *LCDP* shown in Eq. 29 were calculated for each of the Mach Number and angle of attacks pairs. [7]

$$C_n\beta\ dynamic = \left(\frac{dCn_{Body}}{d\beta}\right) * cos\ (\alpha)\ - \left(\frac{dCl_{Body}}{d\beta}\right) * \left(\frac{I_{zz}}{I_{xx}}\right) * sin\ (\alpha) \qquad \text{Eq. 28}$$

$$LCDP = \frac{dCn_{Body}}{d\beta} - \frac{dCl_{Body}}{d\beta} * \frac{\left(\frac{dCn_{Body}}{d\ aileron}\right)}{\left(\frac{dCl_{Body}}{d\ aileron}\right)} \qquad \text{Eq. 29}$$

Now the *LCDP* and *Cnβ dynamic* at the flight condition is required so double interpolation is performed again. This time the known independent variable is the flight angle of attack. Using this angle of attack a similar process described above was utilized with an upper and lower values of *LCDP* and $C_n\beta\ dynamic$ being calculated through interpolation

and then a final interpolation between the upper and lower bounds of those two values using the flight Mach Number. Using the calculated flight $C_n\beta\ dynamic$ the Dutch Roll frequency could then be calculated using Eq. 30.

Due to the commercial nature of our mission another aspect that was of great interest was the lateral directional stability of the aircraft. With the non-traditional mass moments of inertia and high-speed flight this area of flight was of high concern. To determine if the aircraft is prone to control coupling, the Bihrle-Weissman chart is used shown in FIGURE 4 [2]. By plotting *LCDP* and *Cnβ dynamic*, lateral-directional stability characteristics of the aircraft were obtained. The aircraft must remain firmly in the A-region to demonstrate high resistance to spin and departure from stable flight.

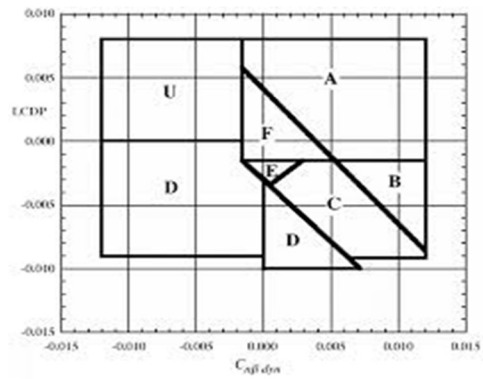

FIGURE 4 - Bihrle-Weissman Chart [2]

$$\omega_{DR} = \frac{1}{2\pi} * \sqrt{\frac{\left(57.3 * C_n\beta\ dynamic * q * S_{ref} * b\right)}{I_{zz}}} \qquad \text{Eq. 30}$$

I. Take-off and Landing Performance

This tool takes in configuration data, an *EDET* output file, and engine data, and returns information on the critical field length (*CFL*) in dry and wet conditions (Eqs. 31-34), one-engine inoperative climb gradient (*OEI ROC*) (Eq. 35), and the *V2* & *VREF* (Eqs. 36-37) speeds in Mach, KEAS, and KTAS at sea level [19, 20].

$$CFL_{DRY} \approx max(750 + 30TOP_{25}, 3000) \qquad \text{Eq. 31}$$

$$CFL_{WET} \approx max(500 + 35TOP_{25}, CFL_{MIN}) \qquad \text{Eq. 32}$$

$$CFL_{MIN} \approx 7700 - 125VMCA + 0.928VMCA^2 \qquad \text{Eq. 33}$$

$$TOP_{25} = \frac{\frac{W}{S_{ref}}}{CL_{max}\frac{T}{W}} \qquad \text{Eq. 34}$$

These calculations involve an empirical estimate of the required landing distance, which is heavily dependent on the wing loading, thrust-to-weight ratio, maximum lift coefficient, and the minimum control airspeed.

$$ROC \approx \frac{T - D}{W}V \qquad \text{Eq. 35}$$

$$V_2 = max(1.13V_{stall,t\backslash oflaps}, 1.1VMCA) \qquad \text{Eq. 36}$$

$$V_{REF} = 1.23V_{stall} \qquad \text{Eq. 37}$$

This mission requires supersonic flight, which is not allowed over the land in the United States; 14 CFR § 91.817 [1]. Therefore, it is assumed that takeoff occurs at or reasonably near sea level so that the mission can achieve supersonic flight over the ocean. For this reason, the tool calculates expected takeoff and climb gradient parameters assuming that altitude is low. This tool was important for the validation of airport compatibility.

J. Fuselage Skin Thickness Chooser

To fully inform the weight estimation, as well as confirm an acceptable level of safety for passengers, the fuselage skin thickness was mathematically determined. Our method uses information from the standard atmosphere for determining static pressure, which was used in combination with the relevant 14 CFR §25.841 for compliance with the pressurization of the cabin. The Hoop stress equation (Eq. 38) was then utilized to find the required skin thickness of the fuselage, using material properties within MIL HDBK-5.[21]

$$t = \frac{\Delta P \cdot r}{\sigma} \qquad \text{Eq. 38}$$

From requirements for certification from 14 CFR § 25.365 [1], the Hoop stress calculated thickness was multiplied by a factor of 1.33 or 1.67 depending on the design altitude.

K. *ModelCenter*

In order to implement a model-based systems engineering process, the above tools developed fed into a *ModelCenter* model. A configuration control sheet that takes bulk parameters, such as maximum takeoff weight, fuel quantity, number of passengers, fuselage width, mission parameters, and propulsion configuration was integrated. The results of certain tools calculations and processes were used to inform the inputs for tools below, as is visualized in FIGURE 5. From the passenger count, parameters related to seats, and fuselage length were computed. These parameters then go to the *VORLAX* Model Creator tool, which creates a *VORLAX* stability model based on the inputs from the configuration controller, and various geometric parameters. This sheet controls the shape of the aircraft, and feeds the relevant parameters back into further sheets, such as the *EDET* model creator and the weight sheet. The *VORLAX* models created by the *VORLAX ModelCenter* tool are used by the stability and control tool, along with the information of the weight sheet to inform the stability picture of our aircraft. The takeoff and landing tool uses information from the stability tool, weight sheet, propulsion configuration and the configuration control sheet to determine takeoff and landing distances for a given configuration. Finally, with the mission parameters and propulsion from the configuration control sheet, the drag buildup from *EDET*, and the weights from the weight tool, along with a mission script are all used by the mission code, which gave our actual mission performance.

FIGURE 5 – *ModelCenter*

IV. Configuration Independent Trades

The proposed mission is significantly different from typical ones because of the ballistic-like portion of the flight. As the plane descends from its peak altitude in an unpowered glide, it will move so fast that atmospheric heating at leading edges could become significant. If heated enough, the leading edges could deform and melt. Furthermore, to achieve the desired altitude, the rocket fuel must occupy a significant fraction of the overall weight at ignition time. Total weight has a significant impact on many operational aspects of an aircraft, including takeoff and landing distances, efficiency, and more. To make informed decisions about overall design, it was important from the early stages of this study to identify general design choices that would reduce the overall weight and the likelihood of overheating. In this section, we present the early trade studies that were carried out prior to developing our system concept.

A. Minimizing Re-Entry Mach Number Through Wing Size

The purpose of this trade study is to find how wing size affects the maximum value for descent Mach Number during the unpowered glide; see FIGURE 6. Even though the study focuses on the effect on Mach Number, there is a strong relation between heating rates and Mach Number; therefore, they are considered analogous here, and the goal is to identify design choices that reduce the maximum descent speed. In this study, wingspan and inner chord length are systematically varied, and the different designs are run through the systems engineering model described in Section III.

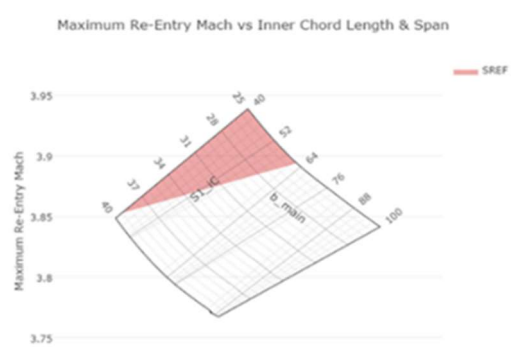

FIGURE 6 – Mach vs Chord Length vs Span

In this study, wingspan was considered over a range of 40 to 100-ft, and the root chord length was considered over a range of 25 to 40-ft. It is important in other parts of the mission to have a wing area of at least $800-ft^2$, so a constraint was imposed to color in red all cases where the wing area is not sufficiently large. By inspection of FIGURE 6, wings that are large in root chord length and wingspan minimize the maximum re-entry Mach Number. Analysis of the trade study data also reveals how each individual design parameter affects the considered performance parameter. This study shows that the average reduction in Mach Number per foot of added span length is 0.002-/ft, and that the average reduction in Mach Number per foot of added chord length is 0.006-/ft.

This study reveals that a wing large in both span and chord length will minimize the maximum re-entry Mach Number. However, it also reveals that the root chord length will have a more significant effect than span. Therefore, this study indicates that a delta-type wing, or one like it, might be the best choice for reducing the descent speed, and associated heating rates. Where possible, inner chord length has been maximized in this design in accordance with the results of this study.

B. Minimizing Re-Entry Mach Number Through Wing Shape

The purpose of this trade study is to find how wing shape affects the maximum value for re-entry Mach Number during the unpowered glide. As before, the descent Mach Number is considered in place of associated heating rates. In this study, wingspan and sweep are systematically varied, and the different designs are run through the systems engineering model described in Section III. Wingspan is considered here to provide a baseline of comparison between the effect of sweep angle and the results presented in Sub-section A. The results of this trade study are shown in FIGURE 7.

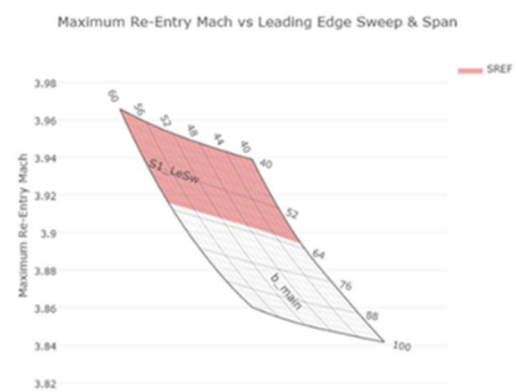

FIGURE 7 - Mach vs Sweep vs Span

In this study, wingspan was considered over the range of 40 to 100-ft, and sweep angle was considered over the range of 40° to 60°. By inspection of FIGURE 7, it is clear that smaller sweep angles lead to reduced re-entry Mach Numbers; however, the effect of sweep angle is substantially smaller than the effect of wingspan. By calculation, the average reduction in Mach Number per reduction of sweep angle is $0.001-deg^{-1}$.

This study shows that the effect of sweep angle on re-entry Mach Number is not as significant as the effect of wing size. Therefore, other design decisions could dictate the sweep angle, and only marginal gains or losses would be had with respect to the maximum re-entry Mach Number. In any case, sweep angle should be minimized if possible.

C. Minimizing OEW Through Wing Size

The purpose of this trade study is to find how wing size affects the OEW of the aircraft. Other factors outside the wing will affect the OEW, but this study generally shows how wingspan and chord length contribute to OEW; see FIGURE 8.

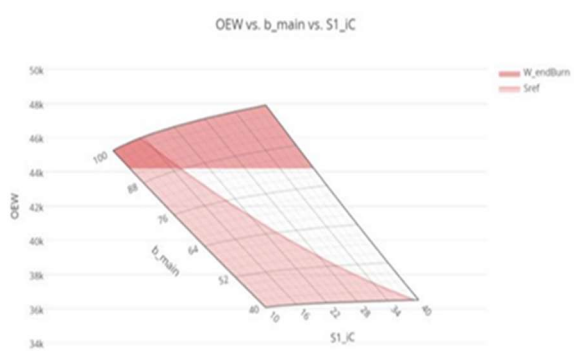

FIGURE 8 – OEW vs Span

This study varies wingspan and chord length over the same range as in Section A. The same wing area constraint is imposed on these results, along with an additional constraint limiting the weight at the end of the burn. This limit was imposed because it was noticed if the weight at the end of the burn exceeded 48,000-lbm, it would fail to complete the mission, so the upper red region represents a region of failed missions. By visual inspection of FIGURE 8, wingspan contributes significantly to OEW, while the effect of root

chord length is substantially smaller. By calculation, the OEW per foot of wingspan ranges from 154 to 196-lbf/ft, and the OEW per foot of chord length ranges from 10 to 83-lbf/ft, increasing significantly in impact as the wingspan increases.

This study showed that chord length has less of an effect on OEW than wingspan, which is an important finding in light of the re-entry Mach Number wing shape study. Together, these show that increasing chord length maximizes advantageous descent drag characteristics without significantly increasing the overall weight. They also show that increasing wingspan benefits descent drag characteristics at the cost of more weight. Altogether, these studies show that inner chord length should be maximized where possible, and wingspan should be limited in size.

V. Configuration Dependent Trades

When the final configuration was more realized, configuration dependent trades could then be completed. The main focus of these studies was to refine how the aircraft should be flown.

To optimize the trajectory of *Sky Cruiser*, a brute force approach was taken with the commanded angles of attack that were given to the Mission Code. On the ascent portion, the brute force study showed that the more aggressive the angle of attack scheduling, the better the maximum altitude achieved and the higher the time over 100 km was achieved.

A. Time over Von Kármán

To ensure the MOE was met, an analysis of time over the Von Kármán line vs re-entry Mach Number was first completed to further refine the trajectory of the vehicle as shown in FIGURE 9. It was found that to have sufficient time over the von Kármán line, the aircraft would need to re-enter at Mach 3.75 or higher.

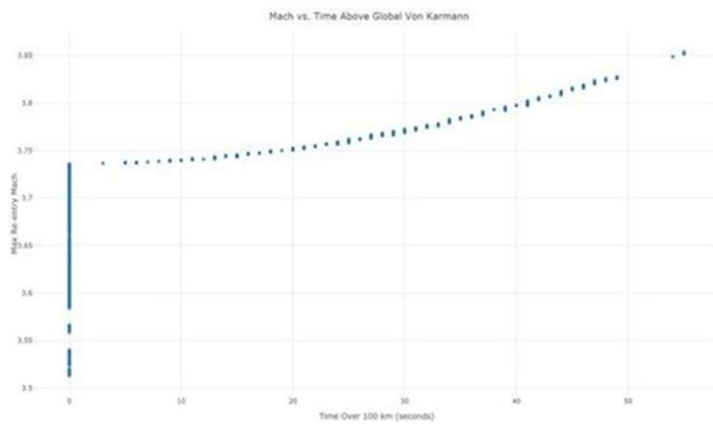

FIGURE 9 – Max Mach Number vs. Time above Global Von Kármán Line

B. Aerodynamic Heating

Due to the speeds and stresses experienced during this flight, there are various considerations that must be made when choosing materials. The aircraft had to be broken down into multiple components since the effects of aerothermal heating vary at different locations along the aircraft. Using the "Mission Performance tool" discussed previously in this article, there were four different temperature measurements that could be evaluated. These include peak stagnation temperature, peak equilibrium wall temperature, reference heating rate, and static temperature. Using the data for each configuration, this can be compared to operational temperature limits from the MIL-HDBK-5 [18]. The thermal properties for each can be seen in TABLE 1.

Table 1: MIL-HDBK5 Material Properties and Corresponding Fuselage Thickness

Material	Max Operating Temperature (R)	Density (lb/in^3)	Ultimate Stress (ksi)	Yield Stress (ksi)	Thickness (in)
2024 Aluminum	1395	0.10	63	42	0.033
7075 Aluminum	1350	0.10	78	70	0.025
Unalloyed Titanium	3494	0.16	80	70	0.025
Advanced Alumina	3556	0.13	58	41	0.033
Polyimide 900 HT	1309	Unknown	Coating	Coating	Variable
Li-900	2760	0.005	Unknown	Unknown	Variable
Alumina Silicate	1932	NA	NA	NA	NA

The studies on stagnation and equilibrium wall temperature revealed that at any Mach Number above 3.65, the peak stagnation temperature is going to be larger than the maximum operable temperature of typical aluminums. The stagnation temperature is nonlinear as shown in FIGURE 10, whereas the equilibrium wall temperature appeared to have a linear relationship with speed as shown in FIGURE 11. Near Mach 4, the wall temperatures come close to the maximum operating temperature of typical aluminum but doesn't exceed it. From this it was determined that the leading edge surfaces of the aircraft cannot be made of aluminum for any of the considered Mach Numbers; therefore, the leading edges of this aircraft will be made of titanium, insulated from the internal aluminum frame by ceramic materials. The skin of the aircraft everywhere else can be made of aluminum so long as the descent Mach Number remains below Mach 4. The maximum Mach Number of the optimum configuration was found to be M 3.75. The corresponding equilibrium wall temperature and stagnation temperature are 1162-^{o}R and 1711-^{o}R respectively.

In addition to temperature selection, there are stresses on the body from flight that must be considered. These were considered using the "Fuselage Thickness tool" and "Wing Thickness tool" discussed previously. These tools include 14 CFR § 25.303, 25.305, 25.365, 25.613, and 25.841 [1] regulations for factors of safety for materials loading. Since the performance of any aircraft is affected by the total mass of the aircraft, the density of the materials is also a primary factor. Using information collected from MIL-HDBK-5 [21] as well as manufacturer specific material information, five materials are considered and compared.

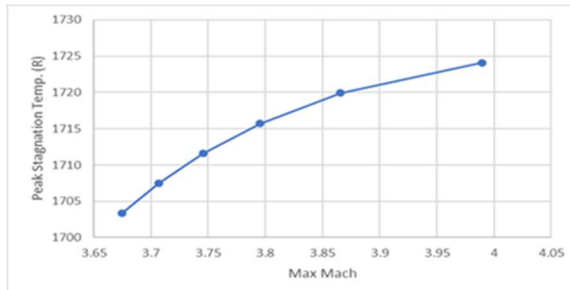

FIGURE 10 – Mach vs Peak Stagnation

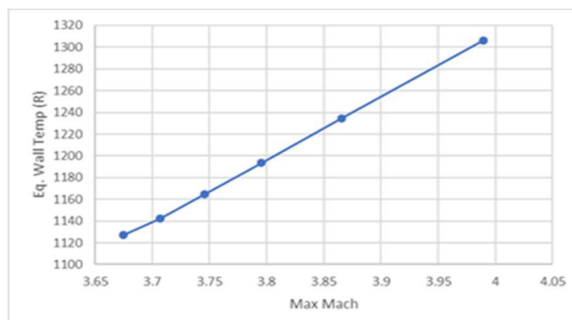

FIGURE 11 – Mach vs Equilibrium Wall

As a result of the studies done and material properties, it was determined that the leading and trailing edges of the wings and control surfaces were to be made of unalloyed titanium. Due to its high operating temperature of 3493-^{o}R, it can withstand the stagnation temperatures that will be generated along the leading edges. Titanium was chosen over advanced alumina based on manufacturing and procurement concerns. Since advanced alumina is made solely by one company, it will be more difficult to obtain compared to the unalloyed titanium which has multiple suppliers. This comes at a sacrifice of some weight but is determined to be an acceptable exchange as the material is only being used for leading and trailing edges. It is also known that aerodynamically, there will be stagnation points on the nose and where the cockpit begins. Due to the shape and manufacturing of the materials, Li-900 was chosen as a suitable, malleable material. Though it has a lower maximum operating temperature than titanium, it is much lighter and more easily manufactured to fit the complex curves along the nose and cockpit. Along with this, Alumina Silicate, 3-pane glass was selected for both the body/passenger compartment and the cockpit windows. This material has been under production for many years and has a maximum operating temperature more than 200 R above the peak stagnation point.

Due to the density, stress limits, and operating temperature it was determined that the remaining parts of the aircraft are to be made of 7075 aluminum. This was chosen primarily for the weight factor as most of the aircraft is to be made of the same material. As seen in TABLE 1, the lower stress limits of the 2024 aluminum cause the skin to be thicker and consequently create a heavier configuration. These thicknesses were evaluated based on the "Fuselage Skin Thickness tool" which considers the CFR requirements previously

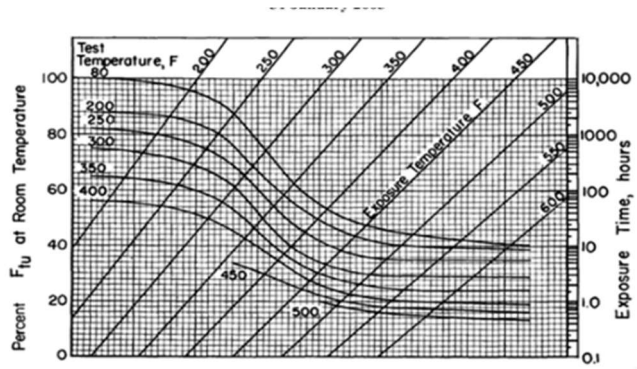

FIGURE 12 – Mach vs Equilibrium Wall Temperature

mentioned. Though the maximum operating temperature of the 7075 aluminum is nearly 200-ºR higher than the max equilibrium wall temperature, there are risks that must be mitigated.

As can be seen in FIGURE 12, the higher the temperature of the aluminum and the more time exposed to higher heats, the lower the percentage of the room temperature yield strength the material will have. Since the highest forces also occur at the highest heats and speeds, a degradation in material performance such as this will pose a major concern to the safety of all aboard the aircraft. To minimize this risk, a layer of polyimide 900 HT is applied to the outer layers of the exposed 7075 aluminum along the fuselage and wings as well as between the outer and inner layers of the fuselage. This material is produced by Nomex/Toray and is already produced for many other aerospace applications. This material can be applied with very thin layers and has an extremely low density thus minimizing weight. It can be reapplied as needed on the aircraft. This resin type layer is designed to keep the underlying material below 300-ºR per manufacturers statements. Though it creates more of a manufacturing and maintenance difficulty, the lower weight benefits compared to an all-titanium body proved more beneficial. The materials used as well as the CFR compliant factors of safety will allow the aircraft to operate over various missions while emphasizing the safety and comfort of passengers and crew.

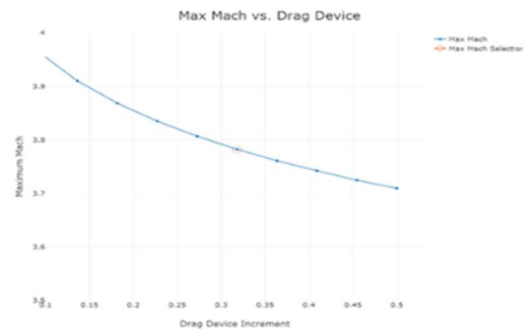

FIGURE 13 – Mach vs Equilibrium Wall Temp.

C. Deployable Drag Devices

It was quickly determined that angle of attack commands on the re-entry portion of the flight did not significantly impact the re-entry velocity of the vehicle, and that the drag device was the most important parameter to consider for the re-entry portion of the flight. This is due to the low dynamic pressure, leading to little induced drag. To determine the amount of drag needed, two trade studies were completed looking at Mach Number dependence and associated *nZmax*. For re-entry into the atmosphere, additional drag devices are needed to obtain the optimum Mach Number. The maximum Mach Number and drag increment associated with it are shown in FIGURE 13. FIGURE 14, shows how the load factor varies with increasing drag increments, this study informed the team that if the drag coefficient was too small, unacceptable load factors were induced on the vehicle, with the potential to cause injury to passenger. Based on these trade studies, the target drag coefficient increment was 0.33, resulting in a required 300-ft^2 of deployable air brakes on the vehicle.

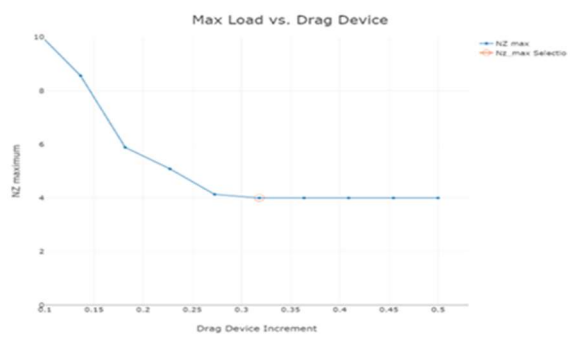

FIGURE 14 – Mach vs Equilibrium Wall

D. Vertical Tail Sizing

Throughout the design process, the sizing of the vertical tail became a key area of concern when looking at the lateral directional stability. To ensure that the aircraft remained stable at high speeds and altitudes numerous iterations of the vertical tail had to be completed to ensure that the aircraft remained within the A region on the Bihrle-Weissman chart. [2] Because the aircraft goes to such a high altitude and dynamic pressure goes to zero, there is no way to avoid the aircraft being in the "F" region during that portion of the flight. During this region of flight any maneuver would need to be made with reaction control system. However, we determined that the benchmark for stability should be at 75,000-ft and Mach 2.5 which is high speed and still in atmosphere.

We found that the limiting case was during re-entry where most of the aircraft mass had been burned off. With each iteration, the vertical tail became larger and larger to ensure that the aircraft was within the "A" region at the benchmark. With the larger tail, crosswind was negatively impacted due to very strong low-speed weathercock stability so that the ailerons and rudders had to sized up to ensure all low-speed CFR requirements were met.

VI. Final Design

A. Wing Final Design

During the analysis of various wing geometries, the resulting c_p* of four control points (CP) of the wing were simultaneously plotted with their upper and lower surface pressure distributions, seen in FIGURE 15. The upper surface pressure coefficients for each airfoil section were closely observed while testing various camber and thickness forms to ensure magnitudes less than that of the corresponding critical pressure coefficient. This ensures that the wing is absent of shock waves at cruise, meaning that it meets its critical Mach Number criterion.

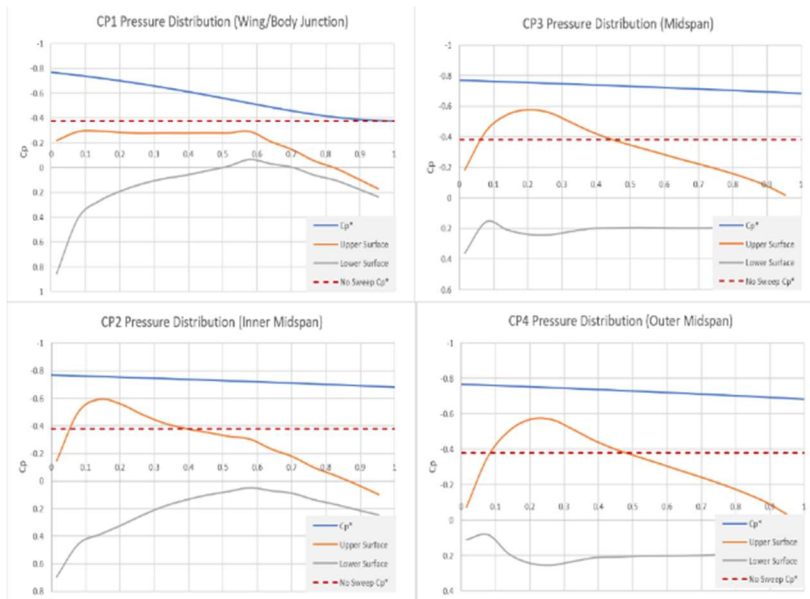

FIGURE 15: Section Pressure Distributions

To minimize *OEW*, wingspan was minimized with more freedom given to chord lengths and sweep. A relatively high sweep angle of 50-degrees was assigned, which was found through *EDET* to give a reasonable buffet lift coefficient and for better Mach performance at high altitudes. As the vertical tail size became larger for high Mach stability, a wing anhedral of 3.5-degrees was included in the design to increase aileron effectiveness and to meet crosswind requirements.

Due to unreasonable or nonexistent stability outputs from *VORLAX*, the tip chord was given a set minimum of about 8-ft, which was adjusted through the root (centerline) chord and taper ratio. To decrease drag, it was considered advantageous to minimize the reference area of the wing, increasing the aspect ratio. Therefore, the centerline chord was assigned a value which minimized reference area but still resulted in a wing loading comparable to aircraft of similar weights, namely a Boeing 737. The thickness forms chosen for each wing section were assigned a thickness percentage (*t/c*) and consisted of a classic NACA 4-digit thickness form with maximum *t/c* at 30% of the chord, along with a NACA 66 thickness form with maximum *t/c* at 50%. Due to the supersonic nature of the proposed mission, the average thickness of the wing was limited to be no greater than 6.5%. The final thickness distribution can be seen in TABLE 2.

Table 2: Wing Thickness Distribution

Location	Thickness Form	t/c %
Side of Body (CP1)	NACA 66	8.5
Inner Midspan (CP2)	NACA 66	6
Midspan (CP3)	NACA 4-digit series	6
Outer Midspan (CP4)	NACA 4-digit series	6
Tip (CP5)	NACA 4-digit series	4
Average Thickness	6.05 %	

The selected NACA 63 and NACA 240 camber lines were then added to the chosen thickness and scaled as needed to achieve the desired pressure distribution and lift for each panel. At the root and inner midspan, the NACA 66 thickness profile was chosen. While this shift in maximum thickness further from the leading edge led to more isobar unsweeping on the Yehudi panel, this was considered preferable since it brought the upper

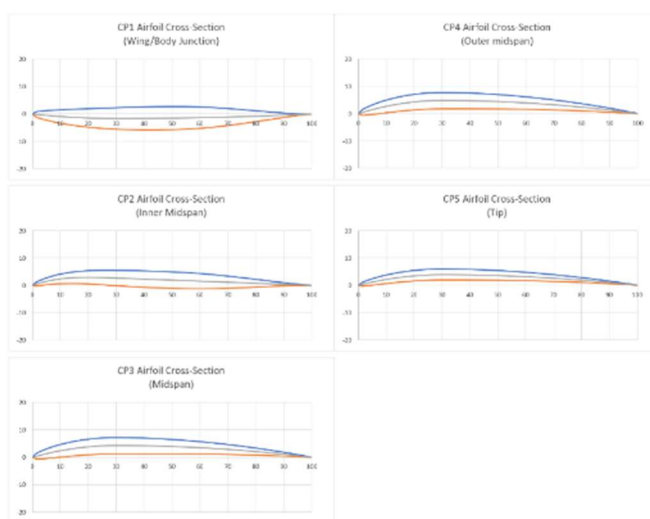

FIGURE 16: Wing Airfoil Geometry

surface pressures below the no sweep c_p*, a consequence not seen from the NACA 4-digit thickness form. A 4-digit thickness profile did prove to be preferable in the outboard panels, specifically near the tip, as it delayed unsweeping of the isobars in this region. The NACA 63 camber form produced isobars parallel to the leading edge across the majority of the upper surface. The "droopier" NACA 240 camber at CP2 (FIGURE 16) provided a small advantage in extending the parallel isobars further towards the side of body, although this advantage was not seen with a NACA 240 camber form at the side of body (CP1).

Table 3: Wing Camber and Twist Distribution

Location	Camber Form	Camber Form %	Camber Max z/c %	Twist (deg)
Side of Body (CP1)	NACA 63	-27	-1.62	8.5
Inner Midspan (CP2)	NACA 240	140	2.912	6
Midspan (CP3)	NACA 63	70	4.2	2
Outer Midspan (CP4)	NACA 63	80	4.8	0
Tip (CP5)	NACA 63	65	3.9	-3

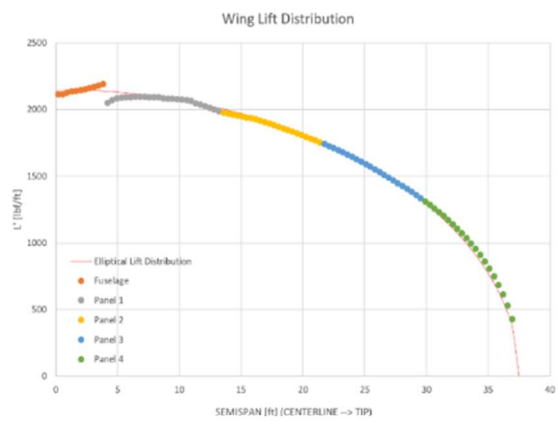

FIGURE 17: Wing Lift Distribution

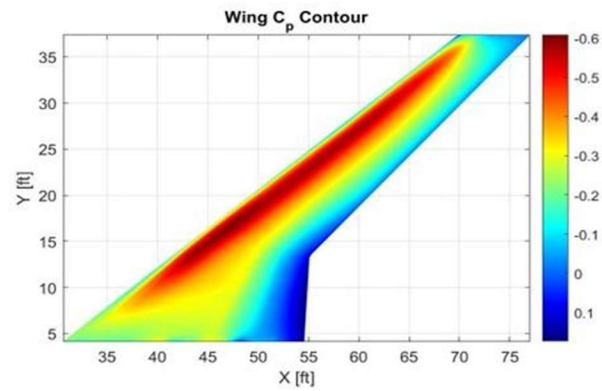

FIGURE 18: Wing Isobars

The lift provided by the fuselage was primarily characterized by the *VORLAX* inputted angle of attack, although its magnitude was also largely controlled by choice of camber and incidence at the side of body. The design span load including effects of the fuselage is illustrated in FIGURE 17. The final design parameters found here yielded favorable isobars, as can be seen in FIGURE 18.

B. Wing Torque Box

The torque box design is largely derivative of the wing design; see FIGURE 19. It is made from 7075 aluminum, the same material as most of the wing.

FIGURE 19: Wing Torque Box

The torque box must be strong enough to satisfy CFR requirements for structural integrity, while allowing sufficient space for control surfaces and jet fuel storage.

The aft placement of the rear spar must be upwind of the control surface hinges. The size of control surfaces is dictated by the stability of the aircraft; in the proposed design, the ailerons and trailing edge devices occupy 30% of the chord outside of the Yehudi. Additionally, 20% of the chord is allocated to leading edge devices and the titanium leading edge. Within the Yehudi, 20% of the chord is allocated to the leading-edge devices, and the torque box connection point is made in such a way that the spar can remain straight from fuselage to the edge of the Yehudi.

The ribs are spaced every 2-ft; their edges are such that with the skin attached, they form the proposed wing design thickness. They are also hollow to allow fuel to be stored within the wing.

C. Air Breathing Propulsion

The air breathing propulsion configuration chosen by the *Sky Cruiser* team was two CFM56-3C1 turbofan engines shown in FIGURE 20. These engines provide 23,500-lbf of thrust and weigh 4,300-lbm each, with a bypass ratio of 6. The CFM56-3C1 provided the best compromise of size, weight, and thrust for the takeoff and climb portions of our flight. The main advantage of the CFM56-3C1 is that it is one of the lighter engines in this thrust class, which was important to allow more weight to be allocated to other areas.

FIGURE 20: CFM56-3C1 Turbofan Engine

The engines were mounted on top of the wings, close inboard of the fuselage, with the engine face at the trailing edge of the wing. This position was chosen for three reasons. First, mounting the engines on top of the wing keeps them out of the line of sight of passengers, allowing for an unobstructed view of the earth from space. Secondly, mounting the engines close inboard reduced the difficulties of one engine inoperative flight. Lastly, mounting the engines at the trailing edge helped kept them over the center of gravity of the vehicle, which helped minimize the center of gravity change before and after 60,000-lbm of rocket fuel was burned in the ballistic portion of the flight trajectory. This aft of the wing position also allowed for integration of ramps that closed the engine off during the ballistic ascent and re-entry of the flight.

D. Rocket Propulsion

The rocket propulsion configuration chosen by the *Sky Cruiser* team was a single Merlin 1D+ shown in FIGURE 21. This rocket is a regeneratively cooled turbopump cycle that is designed for reusability, which was a key design objective for our overall configuration. The rocket provides 190,000-lbf of static thrust at a sea-level and has a specific impulse of I_{SP} = 282-sec. The Merlin 1D+ also has inbuilt thrust vectoring, which is used during the ascent of the rocket portion of the flight to provide control power. The dry weight of this motor is 1,090-lbm. Our design uses the Merlin 1D+ at unitary scale.

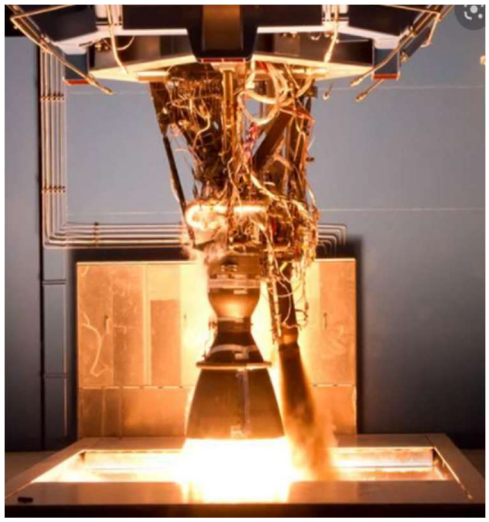

FIGURE 21: Merlin 1D Rocket Engine

E. Fuel Systems

With *Sky Cruiser*'s space tourism mission, a major design driver was the placement and sizing of the rocket fuel tanks. 45.7% of the maximum takeoff weight, 60,000-lbm of propellent, both liquid oxygen (LOX) and RP-1 kerosene-based rocket fuel, was dedicated to achieving 30 seconds over 100 km. In comparison, only 8,800-lbm of regular Jet A fuel was necessary to achieve the air breathing portions of the flight, with 4,600-lbm used to climb up to the ignition altitude, 800-lbm to return to the home runway, and 3,400 to fly to an alternate in emergencies. Jet A fuel takes approximately 1,400-gal of volume and is accommodated in the torque box of the wing. The rocket fuel is stored in two cylindrical tanks with diameters of 77-in. The RP-1 tank is 10.5-ft long and weighs 575-lbm empty, while being capable of carrying 16840-lbm of fuel. It was considered to use Jet A in the rocket portion of the flight; however, the unrefined nature of Jet-A would result in sooty deposits in the regeneratively cooled Merlin 1D rocket. The LOX tank is 19-ft long and weighs 2000-lbm empty; it can store 43,120-lbm of liquid oxygen.

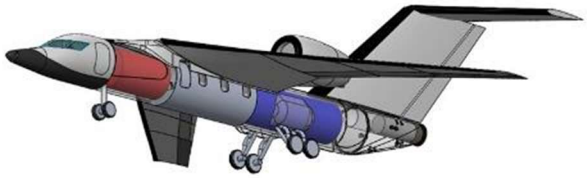

FIGURE 22: Split Fuel Tank Configuration

The tanks are physically separated by the passenger compartment, with the RP-1 tank forward and the LOX tank aft as shown in FIGURE 22. If these tanks were mounted end-to-end, it would result in a large CG shift from pre- and post-burn. Separated, the tank's CG straddles the aircraft CG, resulting in a minimal shift. *Sky Cruiser* is designed to land with full jet fuel, but not any rocket propellant. Both rocket propellant tanks are equipped with separate dumping mechanisms to prevent accidental ignition

Additional safety precautions include the use of fuel dumping procedures in the event of an aborted flight plan. Though the aircraft will retain the required 45-min worth of fuel per 14 CFR § 91.167 [1], the excess rocket fuel including oxidizer and propellant will need to be dumped from the aircraft. Due to the volatility of having large amounts of highly combustible elements when performing emergency operations, it was determined that the excess elements should be dumped prior to landing. The dumping procedure, while not preferred environmentally, ensures that no crash landing or other hazardous accidents will cause even greater destruction than the body of the aircraft itself. This procedure not only aids those aboard the aircraft, but also those who may be within close vicinity in the event of a crash or other accident.

F. Flight Trajectory

Informed by our trade study process, *Sky Cruiser* flies the following mission shown in FIGURE 23 and TABLE 4. The vehicle first climbs at 250-KEAS until it is over 10,000-ft to comply with 14 CFR § 91.117 [1]. After breaching the 10,000-ft limit, *Sky Cruiser* starts climbing at 270-KEAS, which was determined as the optimal climb speed for the MTOW until it reaches 175-nM from Mojave, including a 180° for the aircraft to be facing the coast. At the end of this leg, the aircraft is at 31,000-ft and Mach 0.76. The rocket engine now ignites and accelerates the vehicle to Mach 1.4, whereupon it begins a constant CL climb until reaching 60,000-ft. At this point, the trajectory begins taking scheduled angles of attack, starting at 10° as the rocket gimbles to turn the trajectory skyward. At 80,000-ft, *Sky Cruiser* pitches for 14°. Now the rocket is pitched based on Mach Number. At roughly 175,000-ft and Mach 2.75, *Sky Cruiser* pitches for 20° and begins throttling down to 80%. At 250,000-ft and Mach 3 the rocket throttles down to 60% and pitches to 28°. At 320,000-ft, the rocket pitches to 36° before throttling down completely, 60,000-lbm of rocket fuel having been expended. After this point, *Sky Cruiser* pitches down to 15° using cold gas thrusters where it coasts above the 100-km internationally observed Von Kármán line. At 140,000-ft the air brakes deploy, and the angle of attack gradually returns to 3° as the air breathing engines relight at 30,000-ft and the air brakes are closed. Having traveled 50-nM from the launch point in the ballistic portion of the flight, *Sky Cruiser* cruises another 75-nM at Mach 0.82 and 32,000-ft before beginning its descent towards Mojave. At 10,000-ft, the speed is reduced to 250-KEAS until the aircraft touches down. In the event of emergency, *Sky Cruiser* has enough fuel to fly 50-nM to Bakersfield, CA with a 10,000-ft runway and cruise for 45-min, complying with 14 CFR § 135.223 [1].

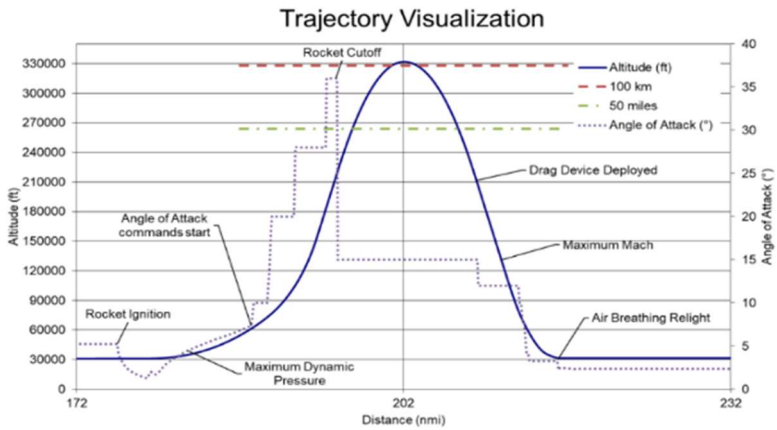

FIGURE 23: Trajectory Visualization

Table 4: Mission Performance Parameters

Apex Altitude	332,000-ft
Maximum Mach	3.76
Time over U.S. Defined Space (50 mi)	129-sec
Time over Karman Line (100 km)	30-sec
Rocket Fuel Consumption	60,300-lbm
Jet Fuel Consumption	9,380-lbm
Peak Stagnation Temperature	1710-R
Peak Equilibrium Wall Temperature	1170-R

FIGURES 24-28 show detailed tracking of key mission parameters with our final configuration. With the primary goal of our mission being to exceed the internationally recognized von Kármán line (328,084-ft), it was with great promise that our vehicle accomplished this for 30-sec, cruising to an apex altitude of 331,800-ft. There is also a period where passengers can experience weightlessness, following the rocket burn. The flight in total from Mojave to space to an alternate airport takes just over two hours to complete, which is comparable in time to many commuter aircraft missions. The maximum values for Mach Number, stagnation temperature, and equilibrium wall temperature are also given in the TABLE 4. These heating values for temperature are within allowable limits for 7075 aluminum on the general body and titanium on the leading edges, especially since these maximum heating values are only experienced for a brief amount of time. The tanks in this aircraft are sufficiently large to hold the fuel required for this mission.

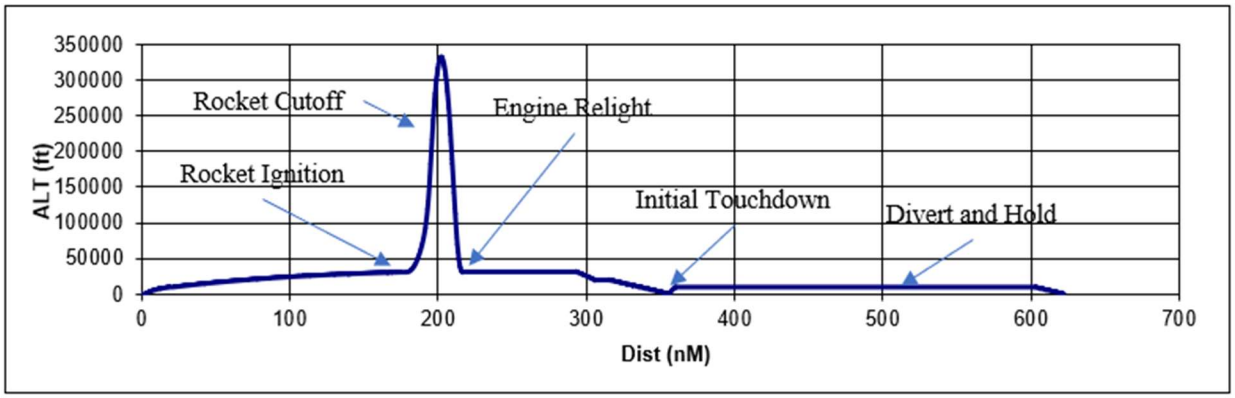

FIGURE 24: Example Mission, Altitude vs. Distance

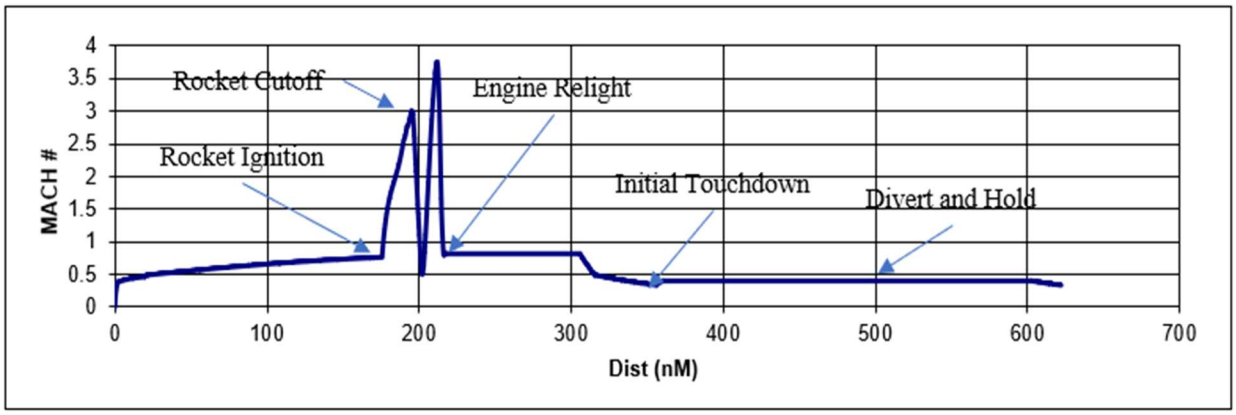

FIGURE 25: Example Mission, Mach vs. Distance

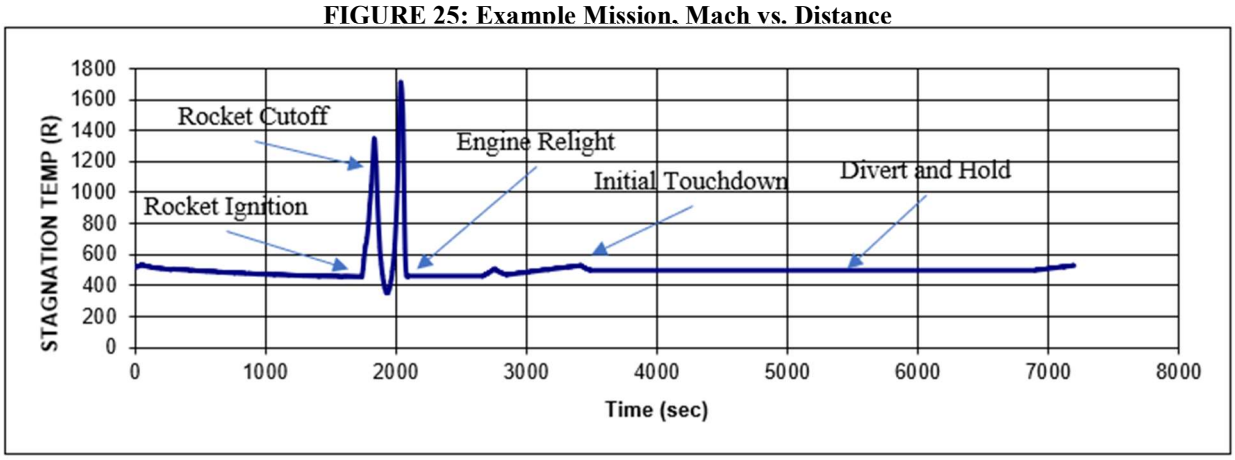

FIGURE 26: Example Mission, Stagnation Temperature vs. Time

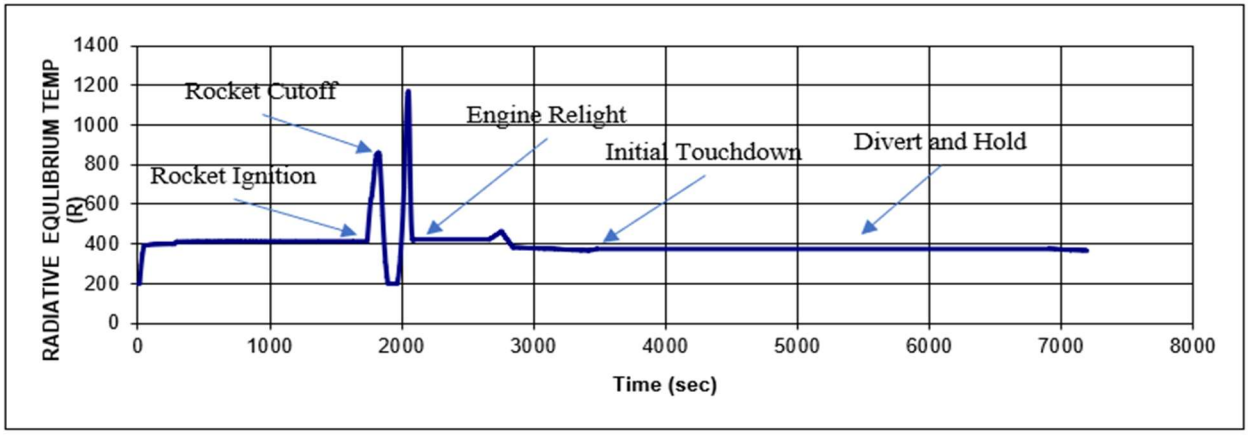

FIGURE 27: Example Mission, Radiative Equilibrium Wall Temperature vs. Time

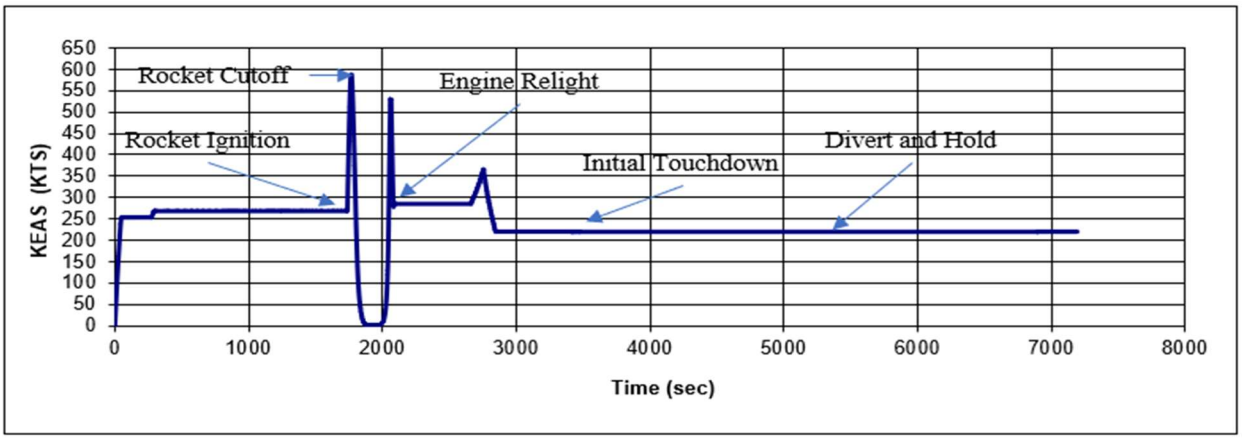

FIGURE 28: Example Mission, KEAS vs. Time

Table 5: Vertical Tail

C_{VT}	.26
c_{root}	25 ft
c_{tip}	18 ft
b_{VT}	18 ft
S_{VT}	333 ft^2
c/4 Sweep	48 deg

Table 6: Horizontal Tail

C_{HT}	.96
c_{root}	12 ft
c_{tip}	8 ft
b_{TH}	28 ft
S_{HT}	280 ft^2
c/4 Sweep	48.5 deg

G. Stability and Control

When sizing the aircraft and determining where the CG should be, there were a few design targets that needed to be hit. The first limitation was the crosswind requirement as stated in 14 CFR § 25. 237 [1], which was one of the main drivers for the sizing of the ailerons. The next limitation was the static margin of the aircraft. With the aircraft going supersonic, this results in the aerodynamic center being shifted back, increasing static margin. Due to the ballistic like trajectory that the aircraft needs to follow, the horizontal tail needed to be sized to ensure that the re-entry angle of attack could be trimmed. The initial angle of attack for climb in the rocket propelled portion of the mission will be reached through a combination of rocket gimbling and tail deflection. The third factor was the lateral-directional stability which resulted in the vertical tail size being exceptionally large; C_{VT} = 0.26. The dimensions of the tail sizing summary are shown in TABLES 5-6. In the following section the stability and control aspect will be described and the process on how these final values were reached

The weight sheet shown in FIGURE 29, was used to determine the mass of many key components. We used a point-mass representation of the aircraft components to determine the center of gravity location and the mass moments of inertia which are needed for stability and control analysis. This mass properties sheet was broken up into four mass parts: mass, component dimensions, CG location relative to target CG, and mass moments of inertia. For some of the components, the mass moments of inertia for a box were used. For complex

geometries like the wing, *SolidWorks* was used. This method was chosen as it allows component size and shape to be modified quickly. The mass properties of the aircraft are shown in TABLE 7.

Table 7: Mass Moments of Inertia

	Pre-Rocket-Burn	Post-Rocket-Burn
Mass (lbm)	131,000	67,000
Target CG (ft) (from nose)	53	53
CG Location (ft) (from nose)	52.7	54.1
Ixx (lbm-ft^2)	7.68×10^6	7.34×10^6
Iyy (lbm-ft^2)	4.25×10^7	2.80×10^7
Izz (lbm-ft^2)	4.39×10^7	2.93×10^7
Ixx/Izz	0.17	0.25
Izz/Ixx	5.72	4

From FIGURE 30, we determined the lift coefficients of the aircraft at various angles of attack. As the aircraft gets more supersonic the lift curve slope shallows indicating very large decreases in the lift coefficient. One key aspect to note is that *VORLAX* does not capture stall or shockwave formation, therefore those effects are not accounted for in the plot.

OUTPUTS				
W/Sref	121.3	lb/ft^2	MEW	58249 lbm
T/W	0.359		BEW	59049 lbm
CHT	0.961		OEW	59728 lbm
CVT	0.261		MZFW	61728 lbm
			MLW	70000 lbm
STRUCTURAL WEIGHT		37204.1 lbm	MTOW	131000 lbm
W_wing_primary_structure	11903	lbm	% Rocket Fuel	45.76941574 %
W_horizontal_tail	1529	lbm	Payload Weights	
W_vertical_tail	2182	lbm	Commuter	1290 lbm
W_fins	0	lbm	Domestic	1440 lbm
W_fuselage	8173	lbm	Long Haul	1895 lbm
W_nosewheel	803	lbm		
W_mainwheel	4689	lbm	W_rocketFuel	59957.93461 lbm
W_aerocontrol surfaces	2361	lbm	W_jetfuel	11314.11284 lbm
"crud weight"	3164	lbm	W_endBurn	68213.54 lbm
W_insulation	671.9670336	lbm		
W_Propellant Tanks	1726.853746	lbm		
PROPULSION WEIGHT		13555.392 lbm		
W_engines	8668	lbm		
W_nacelles & pylons	3666	lbm		
W_batteries	75	lbm		
W_rocket	1036.162	lbm		
W_space_batteries	110.23	lbm		
SYSTEMS WEIGHTS		7939.357383 lbm		
W_APU	400	lbm		
W_instruments	2334	lbm		
W_Hydraulics	1841	lbm		
W_basic_electrical	1312	lbm		
W_avionics	946	lbm		
W_furnishngs	450	lbm		
W_airconditioner	156	lbm		
W_Mission	500	lbm		
TYPICAL RESIDUALS				
W_unusable_fuel	215	lbm		
W_oil	114	lbm		
W_pilots	350	lbm		

FIGURE 29: Weight Sheet Outputs

FIGURE 31, shows the aircraft is statically stable in pitch. When comparing the lift coefficient to the pitching moment, a negative slope indicates stability as the center of gravity is ahead of the aerodynamic center. As the aircraft goes supersonic, the aircraft becomes more stable.

It can be seen from FIGURE 32, that when the aircraft is operating under its critical Mach Number (1.56), the side force trends to become more negative. Once the aircraft is highly supersonic, the side force begins to trend upward becoming more positive. The more negative the side force is, the greater the restoring force, resulting in more stability.

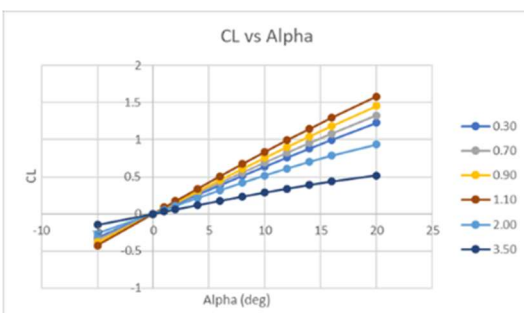

FIGURE 30: Lift Curve Slope

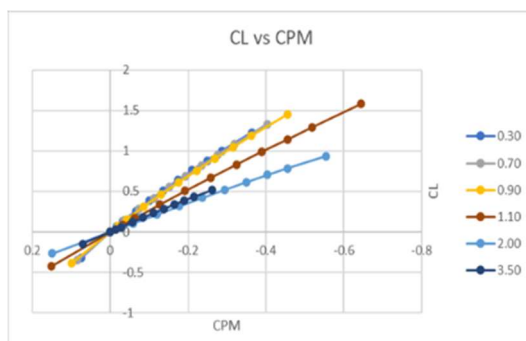

FIGURE 31: Lift Coefficient vs Pitching Coefficient

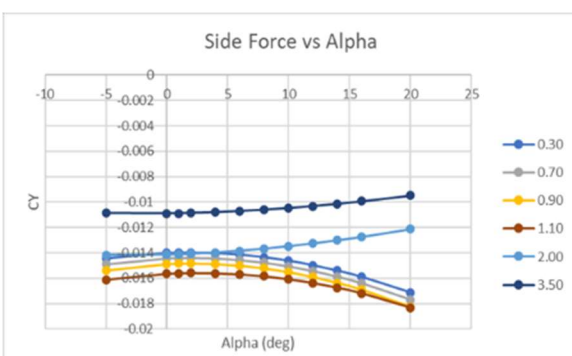

FIGURE 32: Side Force vs Alpha

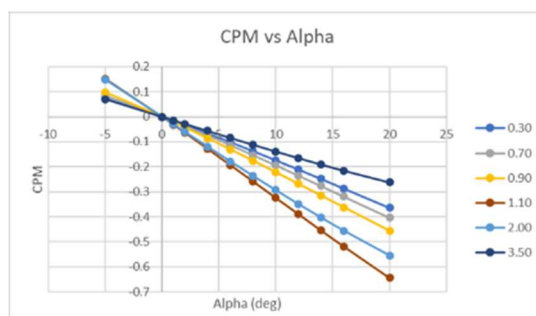

FIGURE 33. Pitching Moment vs Angle of Attack

Next, we will look at the major three plots for stick fixed stability. First, we can see that when the pitching moment curve slope is negative the aircraft is stable in pitch thus, we can determine that the aircraft is stable (FIGURE 33 shown previously). Additionally, with the yawing moment curve slope being positive we can determine that the aircraft is statically stable in yaw as shown in FIGURE 34. This demonstrates that the vehicle has favorable weathercock stability. With the rolling moment curve slope negative it was determined that the aircraft is statically stable in roll as shown in FIGURE 35. This indicates that the aircraft has positive aerodynamic dihedral. As the aircraft becomes more supersonic, the roll stability increases up until after Mach 1.1 where it begins to decrease. This can be seen as the high Mach Number curves are very shallow.

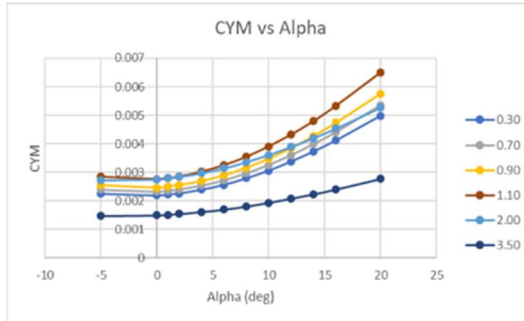

FIGURE 34: Yawing Moment vs Angle of Attack

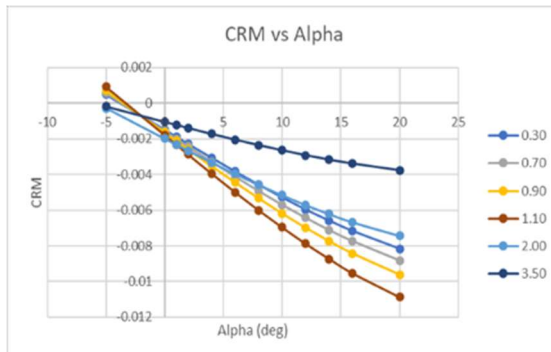

FIGURE 35: Rolling Moment vs Angle of Attack

When looking at the longitudinal stability from the aerodynamic coefficient there were two key parameters of interest, the static margin, and the elevator control power. The static margin is dependent on the center of gravity location and the aerodynamic center of the aircraft. The goal was to balance the center of gravity and aerodynamic center to get the static margin as close to 25% as possible. This would allow for some shift in the CG due to the consumption of fuel. To accomplish this, the wing was moved forward multiple times to get the ideal center of gravity and aerodynamic center locations. This was limited however by the center of gravity and could only move so far forward. As the aircraft goes supersonic, the aerodynamic center moves back resulting the much larger static margins seen in FIGURE 36.

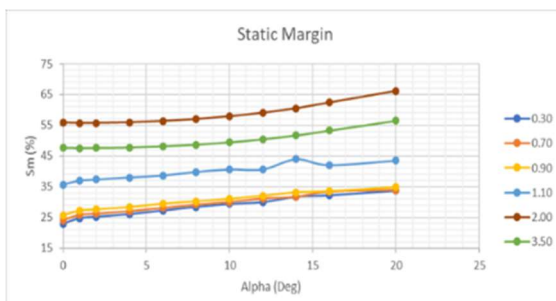

FIGURE 36: Static Margin vs Angle of Attack

Due to the ballistic like trajectory that the aircraft needs to follow, the horizontal tail needed to be sized to ensure that the re-entry angle of attack could be trimmed too. For the mission plan, a re-entry angle of 15-deg needs to be achieved at around Mach 2.6. From FIGURE 37, we can see that the horizontal tail meets this requirement. The initial angle of attack for entry will be reached through a combination of rocket gimbling and tail deflection.

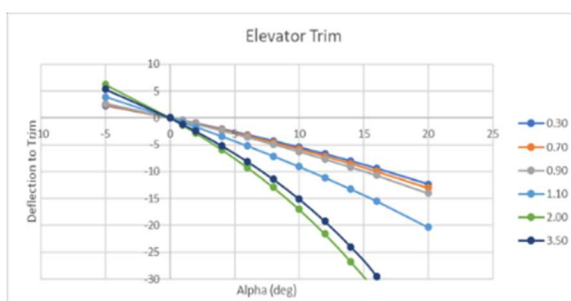

FIGURE 37: Elevator Deflection to Trim

When looking at the yawing moment plots shown in FIGURES 38-39, overleaf, one thing of importance is that we can see that the aircraft is going to be subject to adverse yaw at high Mach Numbers. Adverse yaw occurs when the yawing moment is negative and results in the ailerons producing a yawing moment in addition to a rolling moment which acts as an instability. If the yawing moment is not able to be counteracted, it could cause the aircraft to spin. To remedy this problem, there will be no aileron inputs for maneuvers at high speed. The flight will orient itself to the trajectory beforehand a follow the path. If an emergency maneuver is needed, reaction thrusters will be utilized.

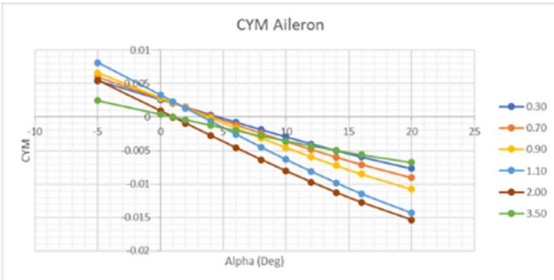

FIGURE 38: Aileron Yawing Moment

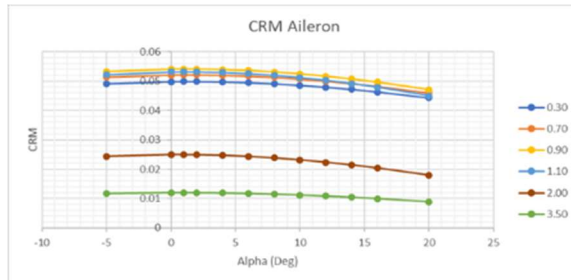

FIGURE 39: Aileron Rolling Moment

When plotting the roll to yaw ratio of the ailerons, shown in FIGURE 40 we can see the ratio of the moments that the aileron will produce. At subsonic speeds for example we can see that the aircraft is producing proverse yaw up until about 4-deg angle of attack, and the yawing moment is only around 10% of the rolling moment. Again, at the supersonic speeds we can see that the ailerons produce commanded adverse yaw that gets up to around 60-80% of the rolling moment. At these conditions, we can see that the ailerons begin to act as a yaw control in a sense. There was not much that could have been done to avoid this as the aileron size was needed to meet the requirements per the CFR.

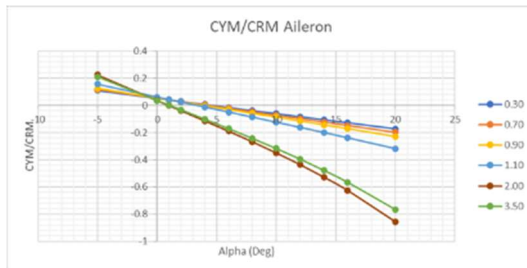

FIGURE 40: Aileron Ratio of Yawing/Rolling

From FIGURE 41, we can see that the rudder loses effectiveness at high speed. This is evident because the subsonic yawing moment coefficient (CYM) for full deflection is around 0.08 but then is reduced to around 0.03 at high supersonic flight. This greatly impacts the ability to trim at supersonic speeds. Again, in the case on an emergency, we plan on using reaction thrusters to complete any trim maneuvers. When looking at FIGURE 42, we can see a similar story, whereas the Mach Number increase the effectiveness trends toward zero. At subsonic speed the rolling moment coefficient produced is around -0.03 and at supersonic speed it declines to -0.005.

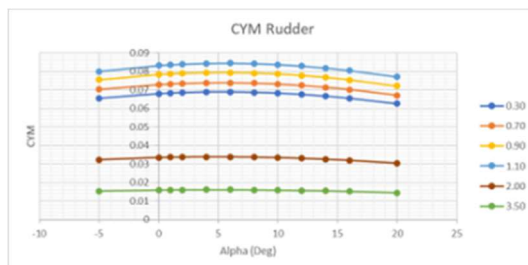

FIGURE 41: Rudder Yawing Moment

When comparing the roll to yaw ratios of the rudder shown in FIGURE 43, we can determine how the rudder will behave. If the magnitude of this parameter is nearly zero, the rudder will function as primarily a yaw control device. If the magnitude of this parameter, however, becomes significantly larger than zero the rudder begins to act as a secondary roll controller like the ailerons. From this we can see that as the Mach Number becomes more supersonic, the CRM/CYM ratio decreases back toward zero. This tells us that as the Mach Number increases, the rudder continues to act as a yaw device indicating it does not need to be locked in place. If the roll to yaw ratio instead became greater, then the rudder would need to be locked as it would further compound the adverse yaw stability problems.

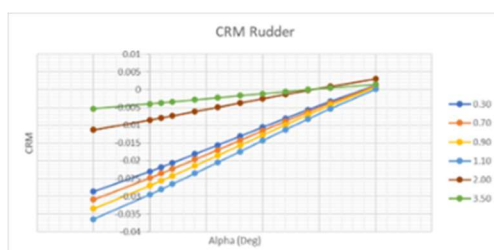

FIGURE 42: Rudder Rolling Moment

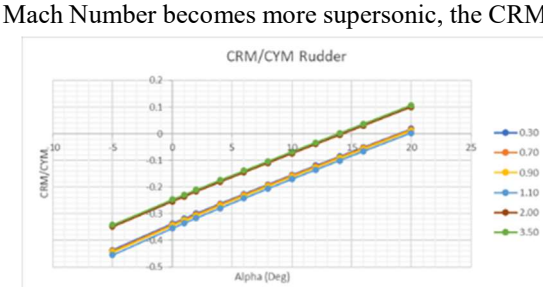

FIGURE 43: Rudder Ratio of Rolling/Yawing

With the all the key coefficients discussed, the next step was to look at the Short Period and Dutch Roll frequencies as well as a few key lateral directional parameters. To conduct the analysis, the flight path shown in TABLE 8 was used in the S&C tool. These key Mach Number and altitude pairs were obtained from the mission code.

Table 8: Flight Profile

Altitude (ft)	Mach	Banked Turn Load Factor
20000	0.620	1
25000	0.690	1
29000	0.755	1
29500	0.800	1
29500	0.860	1
29500	0.950	1
29500	1.180	1
40000	2.000	1
50000	2.250	1
75000	2.500	1
150000	2.900	1
200000	3.000	1

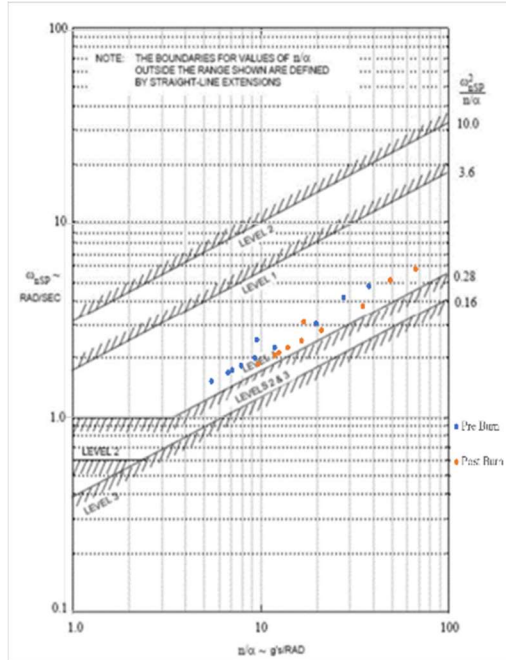

FIGURE 44: MIL STD-8785C for Category A Aircraft

To determine the longitudinal flight handling characteristics, the military standard MIL STD 8785C was utilized. The chart is broken up into three levels each describing the pilot workload. Level 1 is described as having good flying qualities suitable for the mission phase. Level 2 is described as having flying quality characteristics that require more workload out of the pilot which-degrades mission performance. Level 3 indicates that the aircraft is still safe to operate however, the pilot workload is far too much for the mission to be completed effectively.

From FIGURE 44 we can see that during all portions of the flight, the aircraft demonstrates level 1 flight characteristics. On the return, the Short Period frequency did become faster indicating a more responsive aircraft.

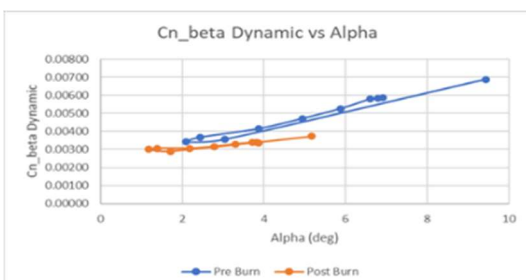

FIGURE 45 A: Cnβ Dynamic Variation

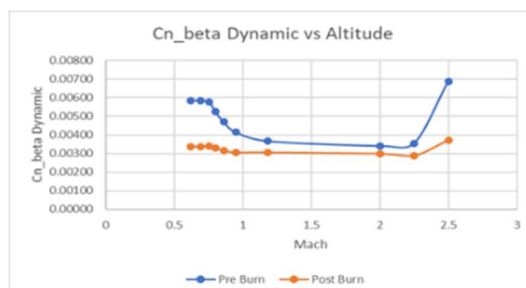

FIGURE 45 B: Cnβ Dynamic Variation

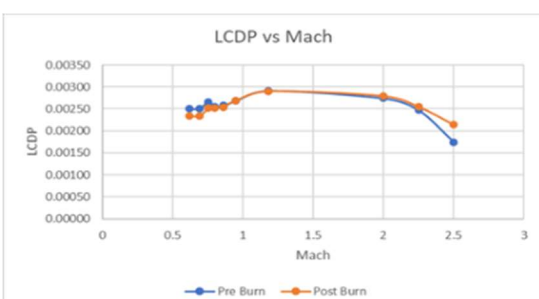

FIGURE 46 A: LCDP Variation

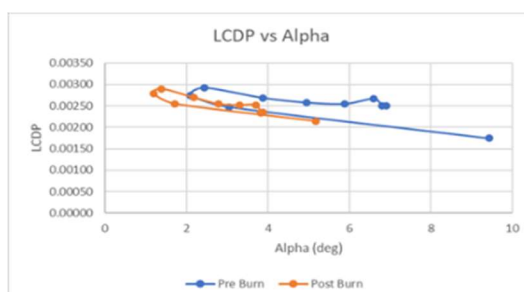

FIGURE 46B: LCDP Variation

Another aspect that was of great interest was to ensure proper lateral directional stability of the aircraft. With the non-traditional mass moments of inertia and high-speed flight this area of stability was of high concern. To determine if the aircraft is prone to control coupling, we use the Bihrle-Weissman chart. By plotting *LCDP* and *Cnβ dynamic*, shown on pervious page in FIGUREs 45 A & B and FIGUREs 46 A & B respectively, we can evaluate the lateral-directional stability characteristics of Sky Cruiser both fully fueled and post burnout. FIGURE 47 demonstrates that the *Sky Cruiser* is inherently departure and spin resistant because all data falls under the "A" region in the Bihrle-Weissman Chart. [7] We note that above 75,000-ft, the dynamic pressure declines to such low values that aerodynamic control surfaces become ineffective and thus were not shown in FIGURE 47.

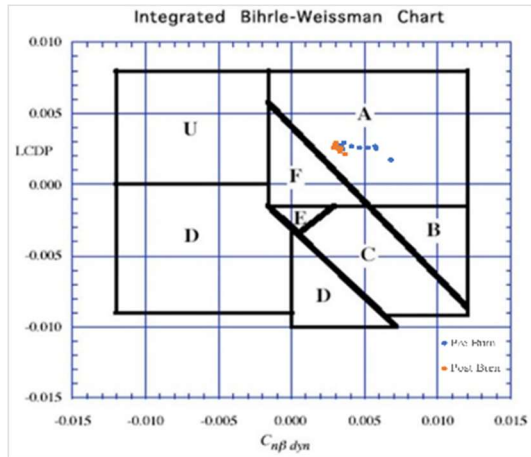

FIGURE 47: Bihrle-Weissman Chart

Next the Dutch Roll frequency is examined, shown in FIGURES 48 A & B. When the frequencies are greater than 0.15-Hz, it can be determined that they are in the "Level 1" flight characteristics zone according to MIL8785-C [3]. We can also see that the frequencies drop to nearly zero at high altitude, which is due to the dynamic pressure heading toward zero. Overall, we can see that the Dutch roll is fastest around the rocket climb segment.

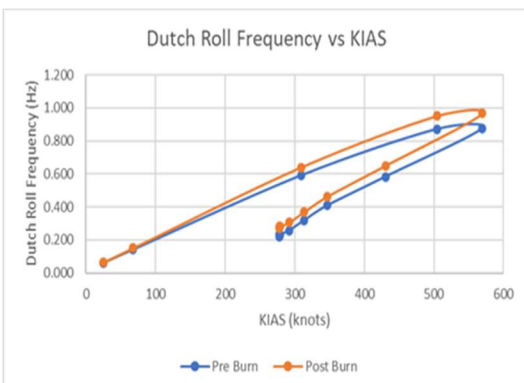

FIGURE 48 A: Dutch Roll Frequency Variation

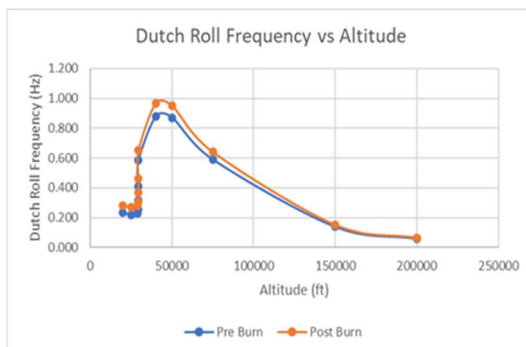

FIGURE 48B: Dutch Roll Frequency Variation

H. Field Performance

TABLE 9 shows the predicted takeoff critical field length and total landing distances for the *Sky Cruiser*.

Table 9: Takeoff and Landing Field Performance

	Half Jet Fuel No Rocket Fuel	Full Jet Fuel No Rocket Fuel	Full Jet Fuel Half Rocket Fuel	Full Jet Fuel Full Rocket Fuel
Weight (lbm)	66,500	73,900	104,000	131,000
α (°)	10	10	15	15
VMCG (KEAS)	97	97	97	97
VMCA (KEAS)	82	83	98	110
Crosswind (KEAS)	26	27	27	31
VMCL (KEAS)	82	82	82	87
V2 (KEAS)	162	171	172	193
V_{ref} (KEAS)	83	100	130	159
CFL_{dry} (ft)	3590	4250	5380	8090
CFL_{wet} (ft)	3810	4590	5900	9060
LDR_{dry} (ft)	1760	2100	2860	3780
115% LDR_{dry} (ft)	2030	2420	3290	4350
167% LDR_{dry} (ft)	2950	3510	4780	6310
LDR_{wet} (ft)	2630	3310	4820	6660
115% LDR_{wet} (ft)	3020	3810	5540	7660
167% LDR_{wet} (ft)	4390	5530	8050	11100

Our planned CONOPS proposes flights originating and returning to the Mojave Air & Space Port. This hub features a 12,503-ft runway. We see in TABLE 9 that, no CFL or LDR with any modifier is greater than this runway length, which means that the proposed plane will be able to operate out of Mojave. Furthermore, the shorter runways at Mojave are 7049-ft and 4747-ft long. Most of the LDR lengths are shorter than these runways, which means that the other runways are adequate at Mojave for landings.

I. Flight Envelope

As discussed in the Skymaps Tool description, *EDET* results in combination with propulsion data were used to generate carpet plots detailing the flight envelope. The specific range results are shown in FIGURES 49-50. Data was generated at both the MTOW and the air-breathing propulsion reignition weight, as the latter is significantly lower than the MTOW due to the sheer volume of rocket fuel burnt, which drastically affects the results detailing the flight envelope. Using these carpet plots, an ideal cruise altitude and Mach Number were found and determined to be 32,000-ft and Mach 0.82.

Additionally, through the Skymaps data (see FIGURES 51-52, overleaf), the climb speed to initial cruise and the speed for landing approach and flight to alternate airport were determined. The optimal climb to cruise was determined to be 270-KEAS, and the most efficient flight to alternate speed was 225-KEAS. It is worth noting that the flight to alternate speed is compliant with 14 CFR § 91.117 [1] which designates the 250-knot speed limit below 10,000-ft.

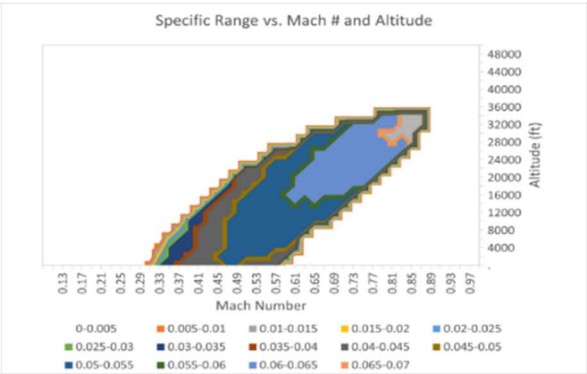

FIGURE 49: Specific Range vs Mach and Altitude, MTOW

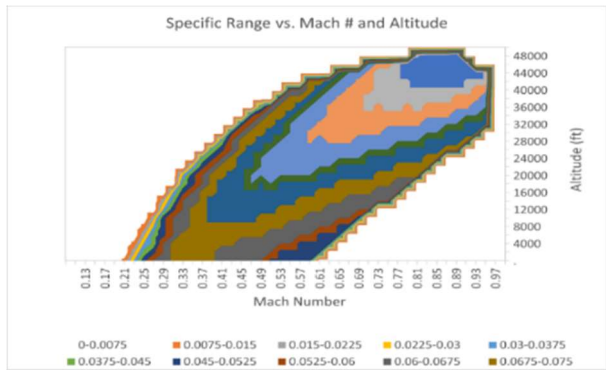

FIGURE 50: Specific Range vs. Mach and Altitude, Reignition Weight

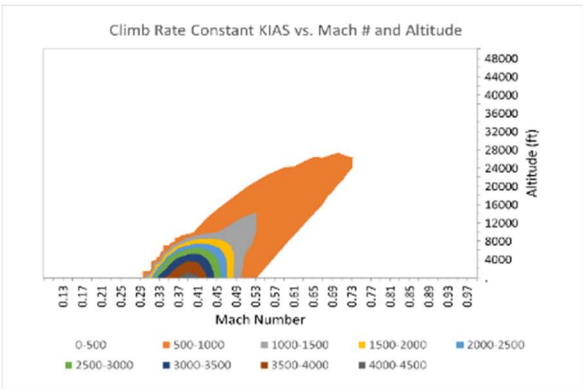

FIGURE 51: MTOW Climb Rate Constant-KEAS vs Mach Number and Altitude

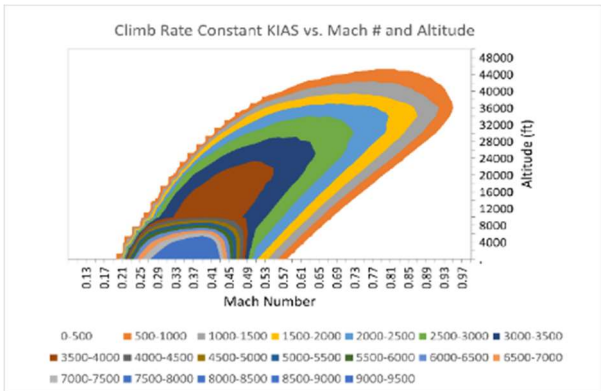

FIGURE 52: Landing Weight Rate of Climb Constant-KEAS vs Mach number and Altitude

Also relevant to the designation of the flight envelope is the *V-N* diagram, seen in FIGURE 53. The positive limit maneuvering load, n, must be 2.5-gees at MTOW. At lighter weights, such as after burnout, the structure can withstand significantly higher maneuvering load factors.

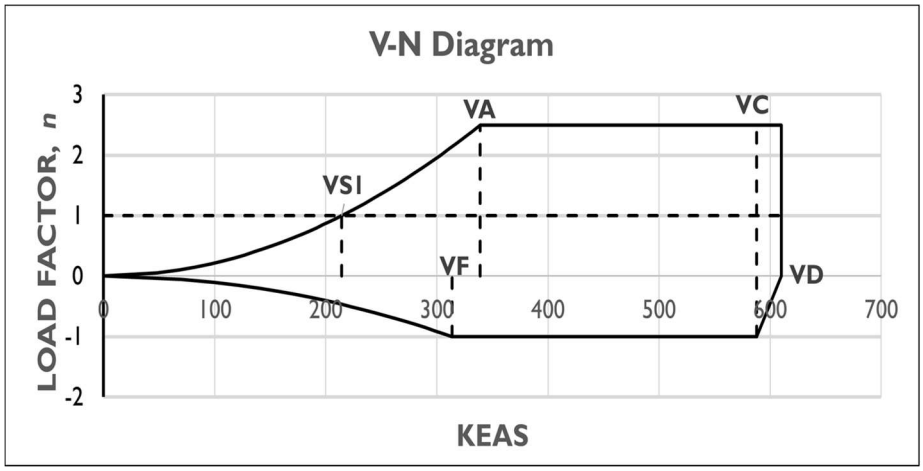

VS1	215 KEAS
VF	314 KEAS
VA	339 KEAS
VC	588 KEAS
VD	610 KEAS
Maximum NZ	2.5

FIGURE 53. *V-N* Diagram

J. Drag Device

Through the trade study conducted on re-entry parameters, it was found that approximately 300-ft$^{2^2}$ of drag brakes were required in order to sustain acceptable load factors and re-entry Mach Numbers. This was obtained through the use of large "petal" air brakes on either side of the fuselage, both fore and aft of the main wing. These air brakes, when combined with a split rudder, much like the space shuttle, provide a combined area of 320-ft², when compared to the overall SREF of 978- ft², these drag brakes provide a drag coefficient of 0.327. This lowers the re-entry Mach Number from over Mach 4 to 3.76, with major decreases in load factor and re-entry heating temperatures.

K. Landing Gear Configuration

The landing gear location and sizing is dependent on various factors including center of gravity (CG) location, tail strike, and take-off and landing performance. According to Roskam [22], it was determined that the rear struts were to be located such that they support 90% of the weight of the aircraft under typical static conditions. This put the landing gear 3.25 ft behind the center of gravity. The front strut is designed such that it is able to support 10% of the weight of the aircraft; see FIGURE 54.

Given the narrowbody design of the aircraft, we found that having four individual struts instead of two for the rear gear configuration would provide greater stability. Using a "canoe" configuration, the rear gear was positioned wider than the relatively narrow fuselage to increase turning ability when on the ground. The canoe configuration also provided additional storage space with sufficient volume to stow the landing gear. This is all reminiscent of the landing gear of a Lockheed C-130. The front gear will rotate 90-degrees and fold forward into the fuselage to avoid hitting the fuel tank behind it.

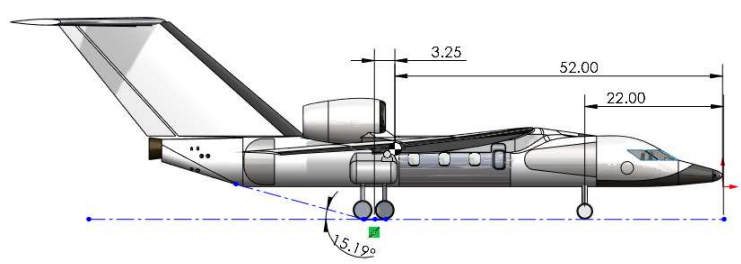

FIGURE 54: Landing Gear with Pre-Burn CG

The height of the landing gear was dominated by the tail strike criteria and the required angle of attack for takeoff. With the takeoff angle of attack at 15-deg, it was found that the landing gear needed to be at least 5.25-ft from the bottom of the fuselage.

Along with gear location requirements, there were additional tire sizing calculations performed. Per 14 CFR § 25.733 [1] requirements, the tires were sized according to the maximum takeoff weight of the aircraft with a 1.07 factor of safety. Given the dual tire configuration on the front gear and the single tire per strut configuration in the rear, the required loads and the selected tires can be seen in TABLE 10. The tires are selected from industry suppliers and are slightly larger than the CFR requirement as to maximize the safety of the aircraft.

Table 10: Tire Sizing

Position	Load per Tire (lbf)	Tire Dimensions (in)	Rated Load (lbf)
Nose gear	21,600	36x11-18	25,000
Main Gear	34,800	30x44.5-14.5	35,800

L. Interior Layout

The layout of the cabin must be CFR compliant, while maintaining sufficient space for passenger comfort. The following CFR requirements must be adhered to by the cabin layout:

14 CFR § 25.815 [1] dictates the width requirements for passenger aisle width. For planes with configurations of 10 or fewer passengers, the aisle width must be at least 12-in. wide at heights less than 25 in. from the floor, and at least 15-in. wide at heights at 25-in. and higher.

14 CFR § 25.785 [1] dictates general requirements regarding seats and safety belts. Each seat must provide sufficient padding to support and protect the passengers. Furthermore, each seat must be equipped with restraining belts.

14 CFR § 25.807 [1] dictates the sizing of emergency exits. For passenger seating configurations of 1 to 9 seats with a wing-on-top configuration, an exit must be provided on each side that meets the requirements of a Type III exit. These exits have a minimum width of 20-in, and a minimum height of 36-in.

These CFR requirements define some of the basic features of the interior layout of this aircraft. The rocket fuel tank is in front of the passenger cabin, and for combustion, the rocket propellant must be piped from the tank, under the floor of the cabin. Raising the floor of the passenger cabin to 24-in from the lowest point of the fuselage allows sufficient space for piping and insulation. This defines the basic planform of the cabin. An additional requirement that must be satisfied is that there must be sufficient space for fuselage skin thickness and for sufficient insulation to protect the passengers from the heat or re-entry. For cabin design, a wall thickness of 4-in was sufficient to cover skin thickness, insulation, and paneling. Finally, there must be sufficient space in the cabin for unobstructed exits.

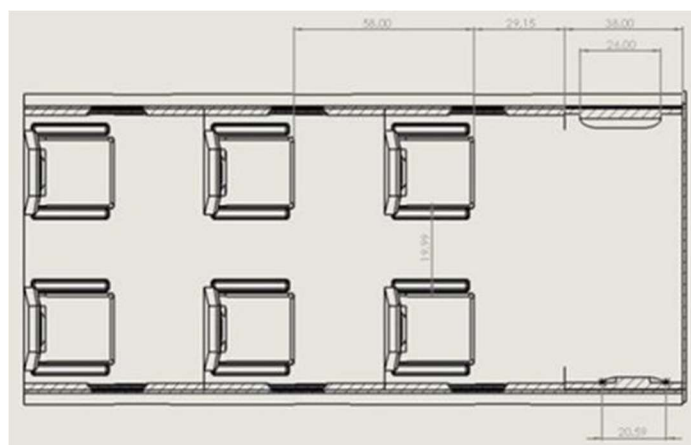

FIGURE 55: Interior Drawing

There are also inferred customer requirements that should be satisfied in the requirements of this cabin. Customers have an expectation that they will be comfortable in the seats they are provided [23, 24]; this leads to a cabin width of 75-in, and the length of 212-in. The seat pitch is 58-in, and the seats are 20-in wide; see FIGURE 55.

VII. Conclusion

Sky Cruiser is a 131,000-lbm, 6 passenger space tourism plane. It is as heavy as it is because it needs to carry 45.7% of its mass as rocket fuel to feed the Merlin 1D rocket engine during its burn. This is to launch above to a maximum altitude of 332,000-ft, loitering in internationally recognized space for 30-sec, and American space for 130-sec. To accommodate passenger visibility, there is a high mounted wing with above the wing mounted engines. For the wide variety of flight conditions encountered from takeoff at sea level to Mach 3.77 at 120,000-ft, a T-tail with a large vertical stabilizer and all moving horizontal tail was chosen to best meet all stability requirements. To take off and

land from Mojave Spaceport, *Sky Cruiser* has a 978-ft^2 wing with a span of 75-ft and two CFM56-3C1 turbofans with 23,500-lbf of thrust each, all to takeoff in 8,088-ft. *Sky Cruiser* is well optimized for its mission. With all aspects considered, our team has developed a configuration that achieves the goals and meets the requirements to design a 14 CFR § 25 [1] certifiable aircraft that leaves the Earth's atmosphere utilizing a mixed propulsion system.

Acknowledgements

This is a refined and evolved version of an undergraduate capstone project performed Fall semester 2021 at Arizona State University. Professor Takahashi wishes to thank Phoenix Integration for their generous support of *ModelCenter* for academic use. The authors acknowledge Zachary Gonzales in the development of the *VORLAX* wing design tool.

Specifications and Drawings

SPECS SHEET						
WEIGHT				***VTAIL***		
MTOW	131000	lbm		Area	333	ft^2
MLW	70000	lbm		Root Chord	25	ft
MZFW	61726	lbm		Tip Chord	18	ft
OEW	59726	lbm		Length	18	ft
FUSELAGE				T/C	12	%
Diameter	8	ft		TR	0.72	
Length	78	ft		Sweep	50	deg
CABIN				% rudder	19	%
Length	17.7	ft		***HTAIL***		
# of pass.	6			Area	280	ft^2
Aisle Wid	20	in		Root Chord	12	ft
Seat Pitch	58	in		Tip Chord	8	ft
WING				Length	28	ft
SREF	978	ft^2		T/C	12	%
W/S	128.8	lbf/ft^2		TR	0.67	
Span	75	ft		Sweep	40	deg
MGC	13.043	ft		% elevator	100	%
TR	0.294			***LOCATIONS***		
AR	5.75			C.G.	54	ft
Avg T/C	6.051	%		Wing-Junc.	40.05	ft
Twist	11.5	deg		Vtail-Junc.	61.25	ft
Sweep	50	deg		Main LG	60.6	ft
% aileron	30	%		Front LG	21.5	ft

Note: Pre-Burn CG at 52 ft with Post Burn- at 54 ft

Design Shock Free Mach	0.82
Design Altitude	32000
Design Dynamic Pressure	270.45 lbf/ft^2
Unit Reynold's Number at Design Point	2183620.67 1/ft
Design Lift	131000-lbm
Fuselage Length	89-ft
Fuselage Diameter	8-ft
Wing/Fuselage Junction (from tip of nose)	30-ft
Design Lift Coefficient (Eq. 9)	0.476
VORLAX Computed Lift Coefficient	0.477
VORLAX Computed Angle of Attack	0.9
Mach Number Normal to the Leading Edge	0.53
Wing Loading	128.81 lbf/ft^2

Span	0.82
Leading Edge Sweep Angle	50-degrees
Trapezoidal Planform Area (S_{ref})	978-ft^2
Trapezoidal Root Chord (at centerline)	18.5-ft
Trapezoidal Tip Chord	7.56-ft
Aspect Ratio	5.75
Trapezoidal Taper Ratio	0.41

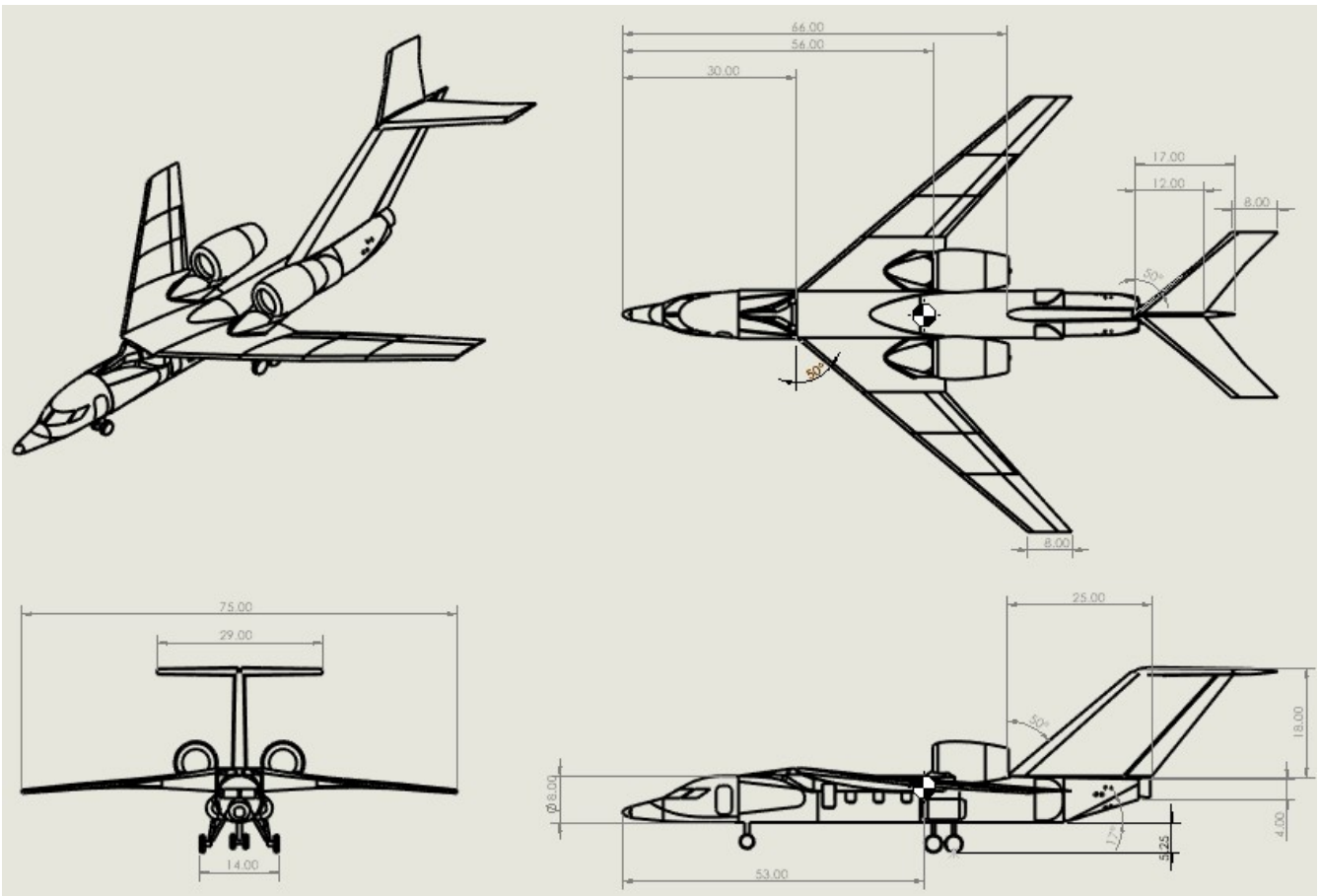

References:

[1] Code of Federal Regulations, General, (2021).

[2] Mason, W.H., "High Alpha and Handling Qualities Aerodynamics," Configuration Aerodynamics Class Notes from Virginia Tech 2018, see: http://www.dept.aoe.vt.edu/~mason/Mason_f/HiAlphaBasicsPres.pdf (accessed November 5, 2021)

[3] Flying Qualities of Piloted Airplanes, MIL STD-8785C, U.S. Department of Defense, Washington, D.C., November 5,1980.

[4] Inc., M., "Spacecraft Thrusters," Moog, Inc. - Precision motion control products, systems, servovalves, actuators Available: https://www.moog.com/products/propulsion-controls/spacecraft/thrusters.html.

[5] Ricard, N., "What type of batteries are better for aircraft and what may be changed in future," DMD Solutions Available: https://dmd.solutions/blog/2019/04/24/what-type-of-batteries-are-better-for-aircraft-and-what-may-be-changed-in-future/.

[6] Torenbeek, E., Synthesis of Subsonic Airplane Design, Delft University Press, Delft, Holland, 1982.

[7] Takahashi, T., Aircraft performance and Sizing: Vol. I and II, New York: Momentum Press, 2016.

[8] Veetil, M.,"Design Methodology for the Performance, Weight, and Economic Assessment of Chemical Rocket Engines," ResearchGate

[9] Berndt, J. S., "Aerodynamic and Properties Data Page for the North American Aviation X-15A," North American Aviation X-15 Available: http://jsbsim.sourceforge.net/X-15.html.

[10] Feagin, R.C., and Morrison, W.D., "Delta Method, An Empirical Drag Buildup Technique," Lockheed-California Co., Rept. LR-27975-VOL-1, 1978.

[11] Miranda, L. R., Elliott, R. D., and Baker, W. M., "A Generalized Vortex Lattice Method for Subsonic and Supersonic Flow Applications," NASA CR-2865, 1977.

[12] Souders, T.J. and Takahashi, T.T., "VORLAX 2020: Benchmarking Examples of a Modernized Potential Flow Solver," AIAA 2021-2459, 2021

[13] Souders, T.J. and Takahashi, T.T., "VORLAX 2020: Making a Potential Flow Solver Great Again," AIAA 2021 2458, 2021.

[14] Griffin, J. A. and Takahashi, T.T., "Aero-Spaceplane Mission Performance Estimations Incorporating Atmospheric Control Limits," Under Review for AIAA AVIATION 2022 Conference.

[15] Küchemann, D., The Aerodynamic Design of Aircraft, AIAA, Virginia, 2012, Chaps. 4, 5.

[16] Kurus, N. J., Takahashi, T. T., and Perez, R. E., "Critical Mach Number predictive methods for realistic supersonic wing / body configurations," AIAA AVIATION 2021 FORUM, 2021

[17] Kirkman, J. J., and Takahashi, T. T., "Critical Mach Number prediction on swept wings," 55th AIAA Aerospace Sciences Meeting, 2017.

[18] Mason, W.H., "1976 Standard atmosphere Subroutine for BASIC" Department of Aerospace and Ocean Engineering, Virginia Tech, 1997

[19] Takahashi, T.T., "Revisiting Roskam's Empirical Predictions for Critical Field Length," AIAA 2021-2446, 2021.

[20] Takahashi, T.T., "Revisiting Roskam's Empirical Predictions for Landing Distance," AIAA 2021-2447, 2021.

[21] Department of Defense. (n.d.). Structural Engineering Research Lab dedicated to steel ... Retrieved December 9, 2021, from http://www.ssrl-uark.com/MILHDBK5H.pdf.

[22] Roskam, J. (2018). Airplane Design. DARcorporation..

[23] Airline Seat Pitch Guide," SKYTRAX Available: https://www.airlinequality.com/info/seat-pitch-guide/.

[24] Are First-Class Airplane Seats Wider? Truth Revealed," Luxury Viewer Available: https://luxuryviewer.com/are-first-class-airplane-seats-wider/.